This is a repository copy of *Ground-based and JWST Observations of SN 2022pul. II. Evidence from nebular spectroscopy for a violent merger in a peculiar type Ia supernova*.

White Rose Research Online URL for this paper:
https://eprints.whiterose.ac.uk/212293/

Version: Published Version

OPEN ACCESS

Ground-based and JWST Observations of SN 2022pul. II. Evidence from Nebular Spectroscopy for a Violent Merger in a Peculiar Type Ia Supernova

Lindsey A. Kwok[1], Matthew R. Siebert[2], Joel Johansson[3], Saurabh W. Jha[1], Stéphane Blondin[4], Luc Dessart[5], Ryan J. Foley[6], D. John Hillier[7], Conor Larison[1], Rüdiger Pakmor[8], Tea Temim[9], Jennifer E. Andrews[10], Katie Auchettl[6,11], Carles Badenes[7], Barna Barnabas[12], K. Azalee Bostroem[13,55], Max J. Brenner Newman[1], Thomas G. Brink[14], María José Bustamante-Rosell[6], Yssavo Camacho-Neves[1], Alejandro Clocchiatti[15,16], David A. Coulter[6], Kyle W. Davis[6], Maxime Deckers[17], Georgios Dimitriadis[17], Yize Dong[18], Joseph Farah[19,20], Alexei V. Filippenko[14], Andreas Flörs[21], Ori D. Fox[2], Peter Garnavich[22], Estefania Padilla Gonzalez[19,20], Or Graur[23,24], Franz-Josef Hambsch[25,26,27,28], Griffin Hosseinzadeh[13], D. Andrew Howell[19,20], John P. Hughes[1], Wolfgang E. Kerzendorf[29,30], Xavier K. Saux[6], Keiichi Maeda[31], Kate Maguire[17], Curtis McCully[19,20], Cassidy Mihalenko[11,32], Megan Newsome[19,20], John T. O'Brien[29], Jeniveve Pearson[13], Craig Pellegrino[19,20], Justin D. R. Pierel[2], Abigail Polin[33,34], Armin Rest[2,35], César Rojas-Bravo[6], David J. Sand[13], Michaela Schwab[1], Melissa Shahbandeh[2], Manisha Shrestha[13], Nathan Smith[13], Louis-Gregory Strolger[2], Tamás Szalai[12,36], Kirsty Taggart[6], Giacomo Terreran[19,20], Jacco H. Terwel[17,37], Samaporn Tinyanont[38], Stefano Valenti[18], József Vinkó[12,39,40,41], J. Craig Wheeler[41], Yi Yang[14], WeiKang Zheng[14], Chris Ashall[42], James M. DerKacy[42], Lluís Galbany[43,44], Peter Hoeflich[45], Thomas de Jaeger[46], Jing Lu[29], Justyn Maund[47], Kyle Medler[48], Nidia Morell[49], Benjamin J. Shappee[50], Maximilian Stritzinger[51], Nicholas Suntzeff[52,53], Michael Tucker[54,56], and Lifan Wang[52,53]

[1] Department of Physics and Astronomy, Rutgers, The State University of New Jersey, 136 Frelinghuysen Road, Piscataway, NJ 08854-8019, USA; lindsey.kwok@physics.rutgers.edu
[2] Space Telescope Science Institute, 3700 San Martin Drive, Baltimore, MD 21218-2410, USA
[3] Oskar Klein Centre, Department of Physics, Stockholm University, Albanova University Center, SE-106 91 Stockholm, Sweden
[4] Aix Marseille Univ, CNRS, CNES, LAM, Marseille, France
[5] Institut d'Astrophysique de Paris, CNRS-Sorbonne Université, 98 bis boulevard Arago, 75014 Paris, France
[6] Department of Astronomy and Astrophysics, University of California, Santa Cruz, CA 95064-1077, USA
[7] Department of Physics and Astronomy and Pittsburgh Particle Physics, Astrophysics and Cosmology Center (PITT PACC), University of Pittsburgh, 3941 O'Hara Street, Pittsburgh, PA 15260, USA
[8] Max-Planck Institute for Astrophysics, Garching, Germany
[9] Department of Astrophysical Sciences, Princeton University, 4 Ivy Lane, Princeton, NJ 08540-7219, USA
[10] Gemini Observatory/NSF's NOIRLab, 670 North A'ohoku Place, Hilo, HI 96720-2700, USA
[11] School of Physics, The University of Melbourne, Parkville, VIC 3010, Australia
[12] Department of Experimental Physics, Institute of Physics, University of Szeged, Dóm tér 9, 6720 Szeged, Hungary
[13] Steward Observatory, University of Arizona, 933 North Cherry Avenue, Tucson, AZ 85721-0065, USA
[14] Department of Astronomy, University of California, Berkeley, CA 94720-3411, USA
[15] Instituto de Astrofísica, Facultad de Física, Pontificia Universidad Católica de Chile, Av. Vicuña Mackenna 4860, Santiago, Chile
[16] Millennium Institute of Astrophysics, Nuncio Monseñor Sótero Sanz 100, Providencia, Santiago, Chile
[17] School of Physics, Trinity College Dublin, The University of Dublin, Dublin 2, Ireland
[18] Department of Physics and Astronomy, University of California, Davis, 1 Shields Avenue, Davis, CA 95616-5270, USA
[19] Las Cumbres Observatory, 6740 Cortona Drive, Suite 102, Goleta, CA 93117-5575, USA
[20] Department of Physics, University of California, Santa Barbara, CA 93106-9530, USA
[21] GSI Helmholtzzentrum für Schwerionenforschung, Planckstraße 1, 64291 Darmstadt, Germany
[22] Department of Physics and Astronomy, University of Notre Dame, Notre Dame, IN 46556, USA
[23] Institute of Cosmology & Gravitation, University of Portsmouth, Dennis Sciama Building, Burnaby Road, Portsmouth PO1 3FX, UK
[24] Department of Astrophysics, American Museum of Natural History, Central Park West and 79th Street, New York, NY 10024-5192, USA
[25] Vereniging Voor Sterrenkunde (VVS), Oostmeers 122 C, 8000 Brugge, Belgium
[26] AAVSO, 185 Alewife Brook Parkway, Suite 410, Cambridge, MA 02138, USA
[27] Groupe Européen d'Observations Stellaires (GEOS), 23 Parc de Levesville, 28300 Bailleau l'Evêque, France
[28] Bundesdeutsche Arbeitsgemeinschaft für Veränderliche Sterne (BAV), Munsterdamm 90, 12169 Berlin, Germany
[29] Department of Physics and Astronomy, Michigan State University, East Lansing, MI 48824, USA
[30] Department of Computational Mathematics, Science, and Engineering, Michigan State University, East Lansing, MI 48824, USA
[31] Department of Astronomy, Kyoto University, Kitashirakawa-Oiwake-cho, Sakyo-ku, Kyoto 606-8502, Japan
[32] ARC Centre of Excellence for All Sky Astrophysics in 3 Dimensions (ASTRO 3D), Australia
[33] Observatories of the Carnegie Institute for Science, 813 Santa Barbara Street, Pasadena, CA 91101-1232, USA
[34] TAPIR, Walter Burke Institute for Theoretical Physics, 350-17, Caltech, Pasadena, CA 91125, USA
[35] Department of Physics and Astronomy, The Johns Hopkins University, 3400 North Charles Street, Baltimore, MD 21218, USA
[36] HUN-REN–SZTE Stellar Astrophysics Research Group, Szegedi út, Kt. 766, 6500 Baja, Hungary
[37] Isaac Newton Group (ING), Apt. de correos 321, E-38700, Santa Cruz de La Palma, Canary Islands, Spain
[38] National Astronomical Research Institute of Thailand, 260 Moo 4, Donkaew, Maerim, Chiang Mai 50180, Thailand
[39] Konkoly Observatory, Research Centre for Astronomy and Earth Sciences (CSFK), MTA Center of Excellence, Konkoly-Thege Miklós út 15-17, 1121 Budapest, Hungary
[40] ELTE Eötvös Loránd University, Institute of Physics and Astronomy, Pázmány Péter sétány 1/A, Budapest 1117 Hungary
[41] Department of Astronomy, University of Texas at Austin, Austin, TX, USA
[42] Department of Physics, Virginia Tech, Blacksburg, VA 24061, USA
[43] Institute of Space Sciences (ICE, CSIC), Campus UAB, Carrer de Can Magrans, s/n, E-08193 Barcelona, Spain
[44] Institut d'Estudis Espacials de Catalunya (IEEC), E-08034 Barcelona, Spain
[45] Department of Physics, Florida State University, 77 Chieftan Way, Tallahassee, FL 32306-4350, USA

[46] LPNHE, (CNRS/IN2P3, Sorbonne Université, Université Paris Cité), Laboratoire de Physique Nucléaire et de Hautes Énergies, 75005 Paris, France
[47] Department of Physics and Astronomy, University of Sheffield, Hicks Building, Hounsfield Road, Sheffield S3 7RH, UK
[48] Astrophysics Research Institute, Liverpool John Moores University, Liverpool L3 5RF, UK
[49] Carnegie Observatories, Las Campanas Observatory, Casilla 601, La Serena, Chile
[50] Institute for Astronomy, University of Hawai'i, 2680 Woodlawn Drive, Honolulu, HI 96822-1839, USA
[51] Department of Physics and Astronomy, Aarhus University, Ny Munkegade 120, DK-8000 Aarhus C, Denmark
[52] Department of Physics and Astronomy, Texas A&M University, 4242 TAMU, College Station, TX 77843, USA
[53] George P. and Cynthia Woods Mitchell Institute for Fundamental Physics & Astronomy, College Station, TX 77843, USA
[54] Center for Cosmology and Astroparticle Physics, The Ohio State University, 191 West Woodruff Ave, Columbus, OH 43215, USA

Abstract

We present an analysis of ground-based and JWST observations of SN 2022pul, a peculiar "03fg-like" (or "super-Chandrasekhar") Type Ia supernova (SN Ia), in the nebular phase at 338 days postexplosion. Our combined spectrum continuously covers 0.4–14 μm and includes the first mid-infrared spectrum of a 03fg-like SN Ia. Compared to normal SN Ia 2021aefx, SN 2022pul exhibits a lower mean ionization state, asymmetric emission-line profiles, stronger emission from the intermediate-mass elements (IMEs) argon and calcium, weaker emission from iron-group elements (IGEs), and the first unambiguous detection of neon in a SN Ia. A strong, broad, centrally peaked [Ne II] line at 12.81 μm was previously predicted as a hallmark of "violent merger" SN Ia models, where dynamical interaction between two sub-$M_{\rm Ch}$ white dwarfs (WDs) causes disruption of the lower-mass WD and detonation of the other. The violent merger scenario was already a leading hypothesis for 03fg-like SNe Ia; in SN 2022pul it can explain the large-scale ejecta asymmetries seen between the IMEs and IGEs and the central location of narrow oxygen and broad neon. We modify extant models to add clumping of the ejecta to reproduce the optical iron emission better, and add mass in the innermost region (<2000 km s^{-1}) to account for the observed narrow [O I] $\lambda\lambda$6300, 6364 emission. A violent WD–WD merger explains many of the observations of SN 2022pul, and our results favor this model interpretation for the subclass of 03fg-like SNe Ia.

1. Introduction

Supernovae (SNe) imprint important information about the composition, geometry, kinematics, and ionization of the ejected material in their late-time (nebular) emission-line spectra. In the nebular phase ($\gtrsim$100 days past maximum light; Bowers et al. 1997; Branch et al. 2008; Silverman et al. 2013; Friesen et al. 2014; Black et al. 2016), the ejecta have expanded and the opacity has dropped enough to see directly through to even the innermost regions and allow forbidden lines to form. In white dwarf (WD) SNe, the decay of radioactive ^{56}Co (produced by the radioactive decay of ^{56}Ni synthesized in the explosion) provides most of the energy that excites the low-density nebular ejecta, producing forbidden emission lines throughout the ejecta (Axelrod 1980; Nadyozhin 1994; Jerkstrand 2017). These glowing ashes contain clues for determining the SN origin. Nebular-phase spectroscopy is therefore an important forensic tool for investigating the remains of exploded WDs, whose explosion channels are not well understood.

The majority of WD SNe are classified as Type Ia supernovae (SNe Ia); however, a growing number and variety of extreme or peculiar SN Ia subtypes have been discovered (for recent reviews, see Taubenberger 2017; Jha et al. 2019; Liu et al. 2023). These peculiar SNe result from the thermonuclear explosion of a WD, but they generally do not follow the Phillips (1993) relationship between luminosity and light-curve

shape that makes normal SNe Ia so useful for cosmological distance measurements (Phillips 1993; Benetti et al. 2005; Taubenberger 2017; Jha et al. 2019). No consensus has been reached concerning the possible and dominant pathways connecting progenitor systems, explosion mechanisms, and observed WD SN properties.

The origins of normal SNe Ia are particularly elusive in part because variations between objects are relatively small and many of the models predict similar observational properties. By contrast, extreme and peculiar WD SNe exhibit distinguishing features that can make identification of their origins clearer (Foley et al. 2013; Kromer et al. 2013; Hsiao et al. 2020). Understanding the scenarios that produce peculiar WD SNe helps us understand the unusual and extreme ways WDs can explode while simultaneously narrowing the model space for normal SNe Ia.

A rare type of peculiar WD SN characterized by high luminosities, broad light curves, C II absorption at early times, relatively low ejecta velocities, and low-ionization state nebular-phase spectra are "03fg-like" (commonly called "super-Chandrasekhar") SNe Ia (Howell et al. 2006; Hicken et al. 2007; Scalzo et al. 2010; Silverman et al. 2011; Taubenberger et al. 2013; Hsiao et al. 2020; Ashall et al. 2021; Srivastav et al. 2023). Explaining the light curve of SN 2003fg, the class prototype, by the decay of ^{56}Ni alone requires a total mass above 1.4 $M_{\odot}$, the Chandrasekhar mass limit ($M_{\rm Ch}$) for a nonrotating WD (Howell et al. 2006). A mass above this limit can be achieved either by additional support from differential rotation in a single WD (Yoon & Langer 2005) or via the merger of two WDs with total mass greater than $M_{\rm Ch}$ (Howell et al. 2006; Hicken et al. 2007). Alternative explanations that have been invoked to explain this diverse class of bright SNe Ia include the "core-degenerate" scenario, where a near-$M_{\rm Ch}$ C/O WD explodes within the C-rich

---

envelope of an asymptotic giant branch (AGB) star (Khokhlov et al. 1993; Hoeflich et al. 1996; Livio & Riess 2003; Quimby et al. 2007; Kashi & Soker 2011; Hsiao et al. 2020; Lu et al. 2021), and the violent merger of two sub-M_{Ch} WDs (Dimitriadis et al. 2022; Siebert et al. 2023; Srivastav et al. 2023). These potential avenues account for the excess luminosity and relatively low velocity of these objects by interaction with the AGB star envelope or C/O-rich circumstellar material (CSM) from the disrupted smaller WD, respectively. For more comprehensive reviews of 03fg-like SNe Ia, see Taubenberger (2017), Ashall et al. (2021), and Paper I (Siebert et al. 2024).

In contrast to the classical WD merger scenario where the merger produces a single-object remnant that later explodes, the violent merger model proceeds via dynamical interaction between two sub-M_{Ch} WDs that causes disruption of the secondary (lower-mass) WD and subsequent detonation of the primary (higher-mass) WD (for a review, see Pakmor 2017). The primary WD is burned first and its ejecta expand beyond the secondary by the time that the secondary is burned ∼1 s later and the ejecta of the secondary expand into the center of the ejecta of the primary. Thus, the intermediate-mass elements (IMEs) produced by burning of the secondary will be centrally located within the ejecta. Depending on the mass ratio, mass of the primary WD, density of the secondary WD at the time of detonation, and composition of both WDs, a fairly wide range of SN properties can be produced (Pakmor et al. 2011, 2012; Kromer et al. 2013; Pakmor 2017). In general, violent mergers are asymmetric scenarios which can result in the enhanced production of IMEs from burning of the secondary, lower levels of iron-group elements (IGEs) from burning of the sub-M_{Ch} primary, centrally located C/O/Ne/Mg and IMEs, and a low-ionization state at late times due to a high central ejecta density.

Nebular spectra can reveal all of these properties. This information can be difficult to disentangle, however, owing to significant line crowding and blending at optical wavelengths. Spectroscopy with JWST in the near-infrared (NIR; which extends beyond the NIR wavelength range accessible from the ground) and mid-infrared (MIR) grants access to emission lines from several species of IMEs, and the lines are comparatively isolated so individual line profiles can be distinguished. These NIR and MIR spectral features help clarify the information contained in the optical and ground-based NIR spectra, aiding in discriminating between progenitor systems and explosion mechanisms. Observations of SN 2021aefx, the first SN Ia with JWST NIR + MIR nebular spectra, revealed strong, stable Ni indicative of a high-mass WD progenitor and evidence for stratified ejecta resulting from some type of detonation (Kwok et al. 2023). Further modeling found SN 2021aefx to be consistent with an off-center delayed detonation of a near-M_{Ch} mass WD (DerKacy et al. 2023).

We obtained a JWST NIR + MIR nebular spectrum of SN 2022pul, a peculiar 03fg-like SN Ia (JWST Cycle 1 GO 2072; PI: S. W. Jha). Our JWST spectrum of SN 2022pul is the first MIR spectrum of a 03fg-like SN Ia, and it exhibits a strong thermal ($T \approx 500$ K) dust continuum (analyzed in Paper III; J. Johansson et al. 2024, in preparation). It also displays several differences from the optical–MIR spectrum of SN 2021aefx. Additional details about SN 2022pul and its unique photometric and spectroscopic evolution can be found in Paper I (Siebert et al. 2024).

Here, we present an analysis of the dust-continuum-subtracted optical through MIR nebular-phase spectrum of SN 2022pul at 338 days postexplosion (this assumes that the dust is external; see J. Johansson et al. 2024, in preparation for a discussion). In Section 2 we identify NIR and MIR emission lines and highlight distinctive spectral properties in comparison to SN 2021aefx. Section 3 presents emission-line-profile fits to the dominant spectral features and their implications on the distribution of material in the ejecta. In Section 4 we compare SN 2022pul to nebular spectroscopic predictions (Blondin et al. 2023) of the violent merger model from Pakmor et al. (2012). We discuss the implications of our results and conclude in Section 5 that SN 2022pul was most likely produced by the violent merger of two WDs.

2. Spectral Analysis

The continuous optical + NIR + MIR spectrum of SN 2022pul in the nebular phase at 338 rest-frame days postexplosion (the estimated explosion date is MJD 59785.3) exhibits many unique properties, including a clear NIR + MIR dust continuum that closely resembles a blackbody (see also Siebert et al. 2024). Here, we focus on an analysis of the spectral lines, while a detailed analysis of the dust properties is given by J. Johansson et al. (2024, in preparation). We remove the dust contribution to the spectrum by subtracting off a blackbody of $T = 500$ K from the 2.5–14 μm region, and use this dust-subtracted spectrum throughout this work. We do not observe other spectral signs of dust such as CO or SiO emission (although line overlap may complicate clear identification of dust extinction in the optical). For details of the observations and data reduction of the spectra used in this work, see Siebert et al. (2024).

Shown in Figure 1, several highlights of SN 2022pul's combined nebular spectrum include a low mean ionization state, strong emission from IMEs, relatively weak emission from IGEs, highly asymmetric line profiles, narrow [O I] $\lambda\lambda6300, 6364$, and remarkably strong [Ca II] $\lambda\lambda7291, 7324$ in the optical spectrum, detection of [S IV] at 10.51 μm, and the first unambiguous detection of [Ne II] at 12.81 μm in a SN Ia.

2.1. Spectroscopic Comparison with SN 2021aefx

SN 2021aefx, a spectroscopically and photometrically regular SN Ia near maximum light, is currently the only other SN Ia with a published continuous spectrum from 0.3 μm to 14 μm in the nebular phase (270 days postexplosion; Kwok et al. 2023), making it a natural comparison object for the peculiar "super-Chandra" 03fg-like SN 2022pul. After subtracting the dust continuum, SN 2022pul has a greater fraction of total flux in the NIR and MIR, and a smaller fraction of optical flux than SN 2021aefx. The light curve of SN 2022pul shows that at late times, the I-band flux exceeds the flux in other bands (probably due to the strong [Ca II] $\lambda\lambda7291, 7324$ doublet) and declines more slowly than typical SNe Ia (Siebert et al. 2024). This is consistent with the findings from Ashall et al. (2021) that 03fg-like SNe Ia are brighter and decline more slowly in the NIR than normal SNe Ia.

This redder color may be due in part to the comparatively low overall ionization state of SN 2022pul, where additional flux from lines of lower ionization falls in the infrared. The flux from optical [Fe III] around 5000 Å is greatly diminished
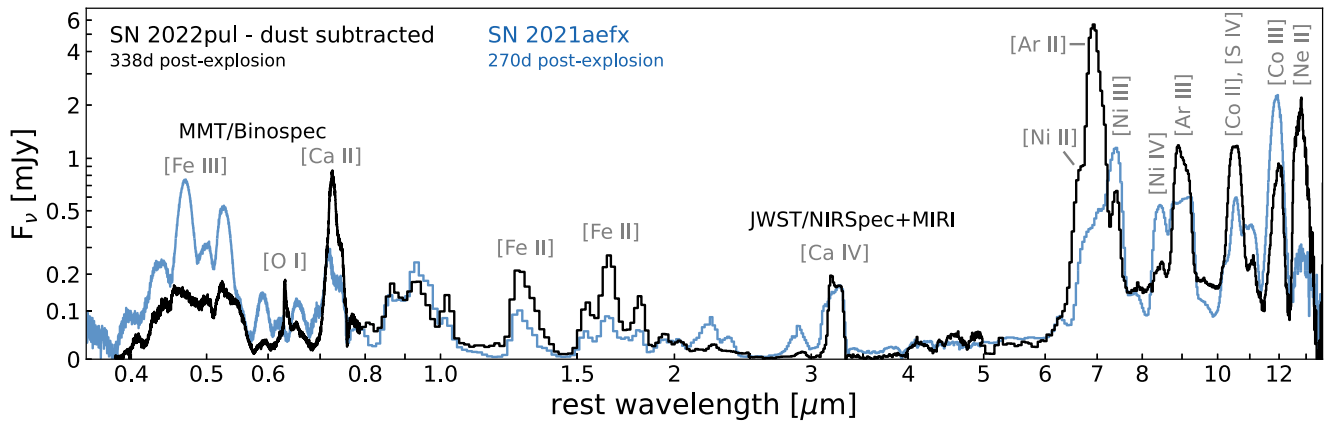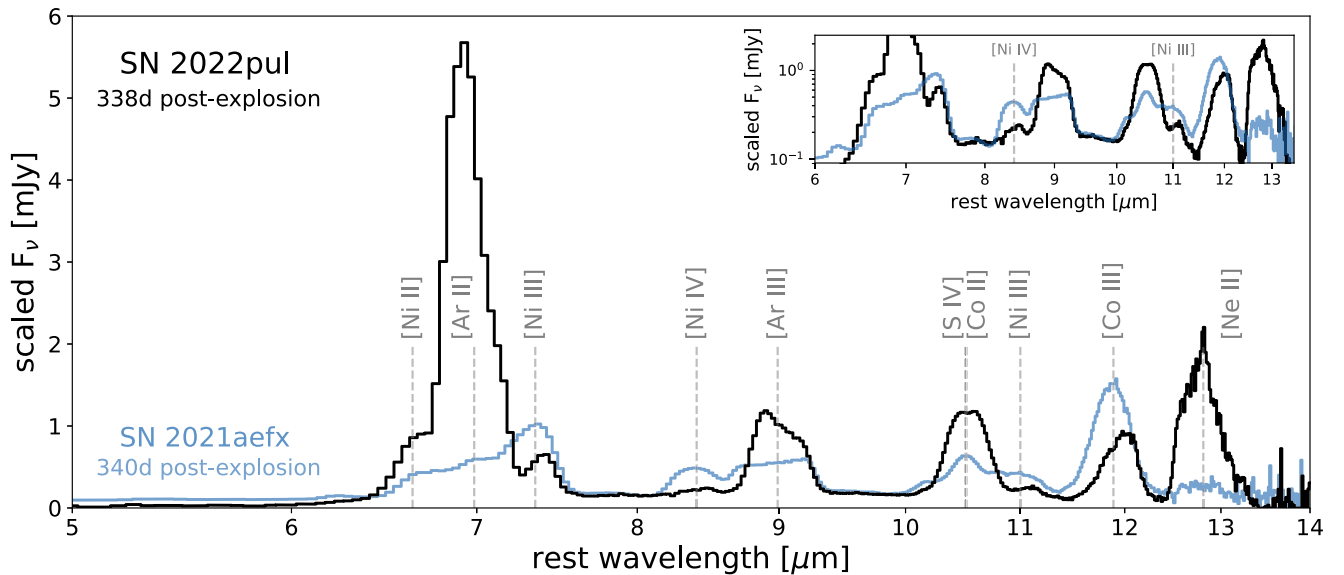
Figure 1. Full optical + NIR + MIR comparison between the dust-continuum-subtracted spectrum of SN 2022pul at 338 rest-frame days postexplosion (t_{exp}= MJD 59785.3) at $d = 16$ Mpc, and SN 2021aefx at 270 days rest-frame days postexplosion at $d = 18$ Mpc from Kwok et al. (2023). The optical spectrum of SN 2022pul is from MMT/Binospec at a similar epoch of 332 days postexplosion and the NIR + MIR spectrum is from JWST/NIRSpec + MIRI. The prominent stable Ni emission lines in SN 2021aefx are weaker (relatively) in SN 2022pul, as is the [Co III] 11.88 μm line. In SN 2022pul, the singly ionized emission lines are relatively strong compared with the higher-ionization states. A strong [Ne II] feature at 12.81 μm is observed in SN 2022pul. The flux axis uses a nonlinear (arcsinh) scale to show better all the features across a wide range of wavelength and F_{ν}.

Figure 2. Comparison between the dust-continuum-subtracted MIR spectrum of SN 2022pul at 338 rest-frame days postexplosion (MJD 59785.3) and the MIR spectrum of SN 2021aefx at 340 rest-frame days postexplosion from DerKacy et al. (2023) scaled to the distance of SN 2022pul (16 Mpc). The prominent stable ^{58}Ni and Co emission lines in SN 2021aefx are somewhat weaker and have shifted to lower mean ionization state in SN 2022pul. The [Ar II] 6.98 μm line dominates the SN 2022pul spectrum, with strong [Ar III] 8.99 μm and [S IV] 10.51 μm as well. [Ne II] at 12.81 μm is strong, broad, and centrally peaked in SN 2022pul. All line profiles are considerably asymmetric. An inset is provided in log scale to show the very weak [Ni IV] 8.41 μm and [Ni III] 11.00 μm lines.

relative to most SNe Ia (Siebert et al. 2024); similarly, the JWST NIRSpec spectrum reveals that the NIR [Fe III] lines around 2.2 and 2.9 μm are weak while the NIR [Fe II] lines around 1.3 and 1.6 μm are strong compared with SN 2021aefx. In the MIR, we see the same ionization trend in Ni, Ar, and Co where the ionization is lower in SN 2022pul than in SN 2021aefx. In agreement with the ionization inferred from the MIR, the strength of the [Ca II] $\lambda\lambda$7291, 7324 doublet in SN 2022pul is remarkable (Siebert et al. 2024), whereas in SN 2021aefx the spectral complex near 7300 Å was attributed to [Fe II] and [Ni II] with little to no contribution from [Ca II] (Kwok et al. 2023), yet they have similar strengths of [Ca IV] near 3.2 μm. This shift to a lower mean ionization for SN 2022pul suggests a larger density or mass of the ejecta, but the presence of Ca IV also indicates that some higher-ionization bubbles are present in both, as discussed further in Section 4.

The NIR does not display lines other than those present in SN 2021aefx, though the [Fe III] is weaker and the three [Fe II] features in the range 4–5 μm are stronger. Blondin et al. (2023) showed that the broad feature near 3.2 μm is dominated by [Ca IV] 3.21 μm, with weaker contributions from [Fe III] 3.23 μm and [Ni I] 3.12 μm. The NIRSpec observation of SN 2022pul further confirms this broad line around 3.2 μm as [Ca IV] 3.21 μm because the [Fe III] and Ni emissions are weaker in SN 2022pul than in SN 2021aefx, but the 3.2 μm feature has a similar strength. Several unique features in the MIRI low-resolution spectrometer (LRS) spectrum of SN 2022pul are shown in Figure 2 and described below.

2.2. [Ne II] Emission

In addition to all of the NIR and MIR lines present in SN 2021aefx (line identifications are given by Kwok et al.
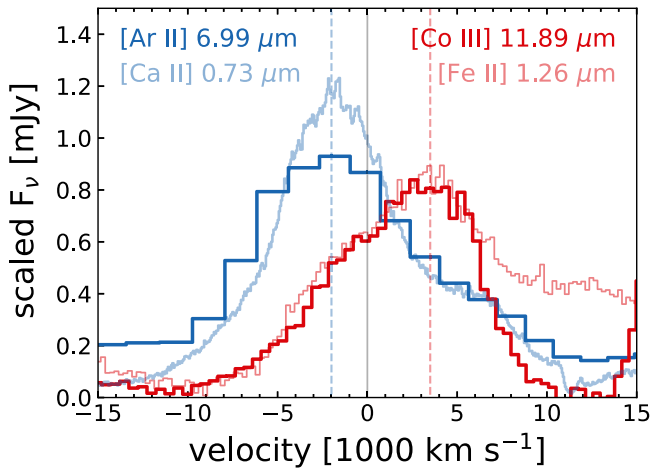
Figure 3. [Ar II] and [Ca II] emission-line profiles in velocity space compared with [Co III] and [Fe II]. The shapes of [Ar II] and [Ca II] are quite consistent with each other, and the shapes of [Co III] and [Fe II] are nearly identical (taking into account the neighboring [Fe II] lines that create the red tail on the [Fe II] 1.26 μm feature). Notably, Ar and Ca (IMEs) have a blueshifted peak with a more extended red tail, while Co and Fe (IGEs) display an opposite trend, with a redshifted peak and a more extended blue tail.

2023), SN 2022pul exhibits a strong, broad, centrally peaked feature around 12.8 μm that we identify as [Ne II] 12.81 μm (see Figure 2). Predicted by Blondin et al. (2023), the presence of strong, centrally peaked [Ne II] 12.81 μm is a distinguishing feature of a violent WD–WD merger not present in any of the other models considered in their study. Ne is produced centrally in a violent WD–WD merger because it is a product of burning the less dense secondary WD, whose ejecta expand into the center of the primary WD's ejecta after the primary has burned and expanded. The observed [Ne II] 12.81 μm line is broad, asymmetric, and dissimilar to other line-profile shapes seen in SN 2022pul and other SNe Ia with MIR spectra.

2.3. Strong Intermediate-mass Elements

One of the major differences between the MIR spectra of SN 2022pul and SN 2021aefx is the strength of the IME (hereafter defined as S, Ar, and Ca) emission lines. Whereas in SN 2021aefx, [Ar II] 6.98 μm was blended out by neighboring Ni emission lines such that its shape was uncertain, [Ar II] 6.98 μm is the dominant emission line in the MIR spectrum of SN 2022pul. Its peak flux is blueshifted by $\sim$2000 km s^{-1}, and is over twice as strong in F_ν as [Ne II] 12.81 μm, the next-strongest MIR emission line. Similarly, [Ca II] $\lambda\lambda$7291, 7324 dominates the optical spectrum.

The [Ar III] 8.99 μm emission line is also quite strong in SN 2022pul: roughly 3 times stronger in F_ν than in SN 2021aefx at a very similar time postexplosion (see Figure 2). The [Ar III] 8.99 μm line continues to exhibit a boxy, flat-topped shape with a similar width, but the slanted top is much steeper. This steep slant can be produced by an asymmetric shell of [Ar III] emission, discussed further in Section 3.

The feature at 10.5 μm in SN 2022pul results from a combination of [S IV] 10.51 μm and [Co II] 10.52 μm emission. The strength and flat shape of the feature at 10.5 μm cannot be explained by [Co II] 10.52 μm alone, as is further discussed in Section 3, constituting a firm detection of [S IV]. Kwok et al. (2023) did not invoke a contribution from [S IV] 10.51 μm in SN 2021aefx; however, placed in context with SN 2022pul, the

"shoulder" feature starting at 10 μm in SN 2021aefx might actually be [Si IV] with a similar boxy shape as the [Ar III] but with about half the strength. Reevaluation of [S IV] in SN 2021aefx will be included in future work.

All of the IME emission lines in SN 2022pul are strong relative to SN 2021aefx, and their peak emission is asymmetric and blueshifted.

2.4. Weak Iron-group Elements

In contrast to the strength of the IMEs, the IGEs (hereafter Fe, Co, and Ni) appear somewhat weaker in the MIR than in SN 2021aefx. Part or all of this apparent decrease in IGEs may be due to the shift to lower ionization. For example, the [Ni II] 6.64 μm line is much stronger in SN 2022pul, but the [Ni III] lines at 7.35 and 11.00 μm are several times weaker, and the [Ni IV] 8.41 μm line is so weak that it is difficult to see without an arcsinh or log scaling of the flux. This points toward some of the flux in the higher-ionization IGE emission lines being shifted to the singly ionized emission lines.

The isolated [Co III] 11.89 μm line shows a distinctly asymmetric shape whose peak is redshifted by $\sim$3500 km s^{-1}. Compared with SN 2021aefx, the [Co III] 11.89 μm line is somewhat narrower. As will be shown and discussed in Section 3, the asymmetric redshifted shape of the [Co III] 11.89 μm line profile is consistent with all of the other IGE ions throughout the NIR and MIR, as well as the redder side of the optical.

3. Emission-line Profiles

Nebular emission-line profiles are important indicators of the geometry of the SN ejecta because they imprint the flux at all projected line-of-sight velocities (and therefore projected radii) through the ejecta. The shapes of the lines arise from a combination of the density and excitation of the elements within the ejecta (for a review, see Jerkstrand 2017). In SN 2022pul, we find evidence in the highly asymmetric line profiles for distinct distributions of the IGEs (Fe, Co, and Ni), IMEs (S, Ar, and Ca), O, and Ne within the ejecta. Unfortunately, it is not possible to determine the full 3D geometry that gives rise to each profile owing to projection effects and the possibility of bubbles, mushroom shapes, clumps, or other such nonspherically symmetric distributions. However, by fitting the line profiles throughout the optical, NIR, and MIR, we can determine the composition within slabs perpendicular to the line of sight, which resolve some of the geometrical layout. In this section we fit line profiles consistently across the optical + NIR + MIR and discuss their implications.

For our line-profile fitting, we need relatively high resolution to discern line-profile shapes, so we combine an optical MMT/ Binospec spectrum at 332 days postexplosion, a NIR Keck/ NIRES spectrum at 316 days postexplosion (the nearest-phase ground-based NIR spectrum available), and the JWST/ NIRSpec + MIRI spectrum beyond 1.83 μm at 338 days postexplosion (Siebert et al. 2024). Despite the difference in phase, we use the Keck/NIRES spectrum (rebinned to increase the signal-to-noise ratio per pixel) instead of the JWST/ NIRSpec spectrum in the range 1.0–1.83 μm owing to its much higher resolution. In addition to removing the dust contribution, we also remove all remaining underlying MIR
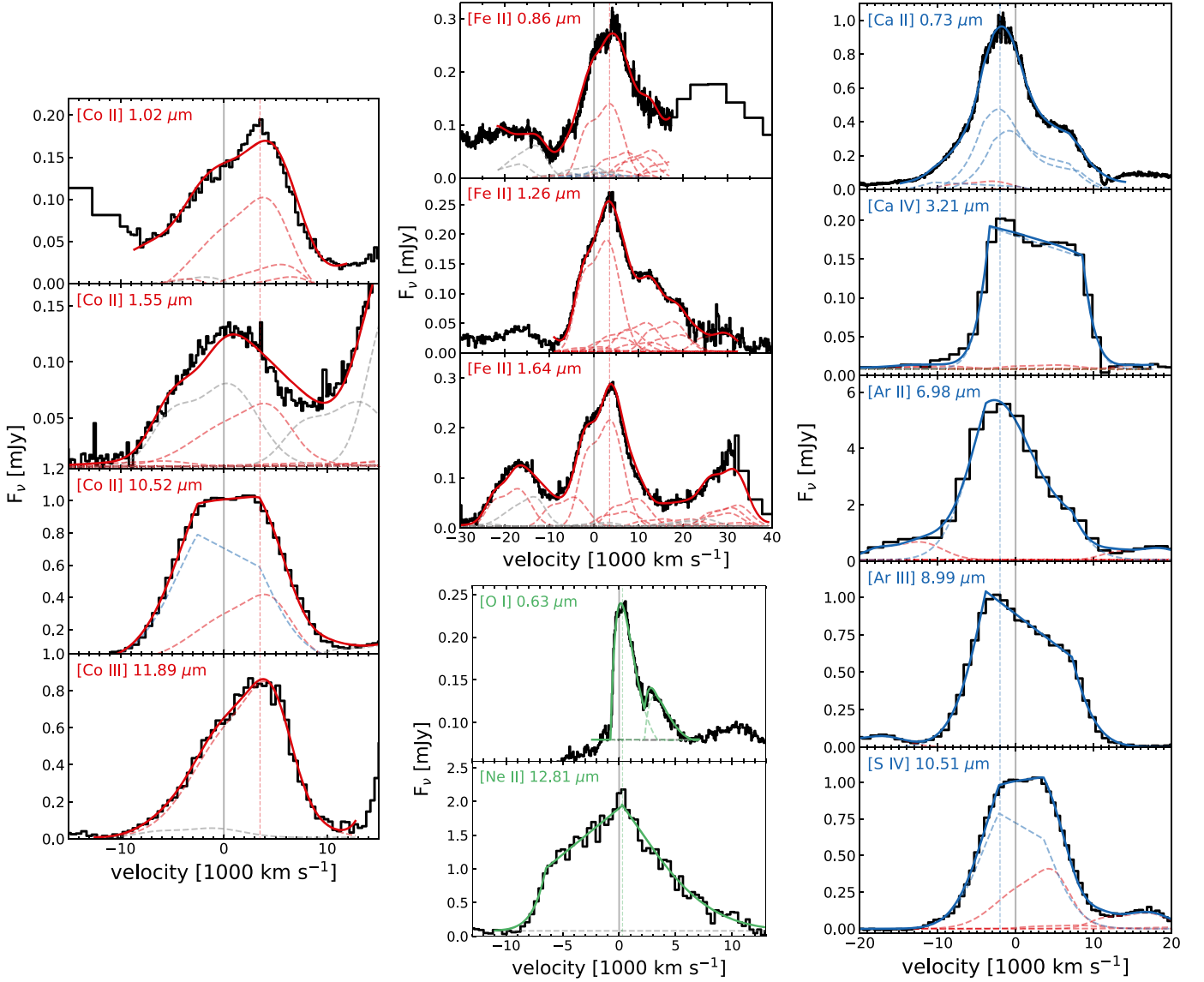
Figure 4. Left: fits to Co emission lines. The vertical dashed red line shows that the peak of the IGE distributions is highly redshifted at ∼3500 km s⁻¹. Neighboring IME lines are shown as dashed blue lines while neighboring Fe lines are given as dashed gray lines. Center top: similar to the Co fits, but for Fe (neighboring Co lines are dashed gray). Right: fits to the IME emission lines. Neighboring IGE lines are shown in dashed red. The vertical dashed blue line shows the peak of the IME distributions, which is highly blueshifted at ∼2000 km s⁻¹. Center bottom: fits to the optical [O I] λλ6300, 6364 doublet and the MIR [Ne II] 12.81 μm line. [O I] is very central and narrow. [Ne II] peaks at the same location as [O I] (vertical dashed green line); however, it has an additional Gaussian-like red wing and a flat-topped-like blue wing slanted in the direction opposite to that of the IMEs.

continuum in the JWST data (see J. Johansson et al. 2024, in preparation, for a discussion of the MIR continuum).

The optical, NIR, and MIR spectra of SN 2022pul are all essential to this work: the higher resolution of the ground-based optical and NIR spectra provides clarity for several key line-profile shapes, and the lower-resolution JWST data contain isolated lines and emission from IMEs. These properties of the data are complementary for interpreting the line profiles of SN 2022pul.

3.1. Line-fitting Procedure

Following the general approach of nebular line fitting from Flörs et al. (2018), Maguire et al. (2018), Flörs et al. (2020), and Kwok et al. (2023), we model the observed spectrum as a superposition of line profiles for all reasonably strong

contributing lines. Restrictions on the fitting are enforced such that all lines of the same ion have the same profile-shape parameters and kinematic offset from the central wavelength. We note similarities between the nebular spectrum of SN 2022pul and the nebular spectrum of the violent WD–WD merger model of Pakmor et al. (2012) computed by Blondin et al. (2023; their MERGER model). Thus, we compute this model out to the same phase as SN 2022pul (338 days postexplosion) and we fix the relative line strengths of each contributing line in our fits to the relative line strengths in the model. This allows us to base the relative line strengths on temperatures and densities similar to those in SN 2022pul. Details of and comparisons to the merger model are presented in Section 4.

While the relative line strengths within a given ion are fixed by the MERGER model at 338 days, we allow the relative

amplitudes between each ion to vary as fitting parameters. We fit the optical through MIR and include the following ions: Fe I, Fe II, Fe III, Co II, Co III, Ni II, Ni III, Ni IV, S IV, Ca II, Ca IV, Ar II, Ar III, O I, and Ne II. Additionally, to account for asymmetry in SN 2022pul, we fit each ion with non-Gaussian line profiles, further described below.

The resolution of the NIRSpec/Prism and MIRI/LRS data introduces significant uncertainties into the fits for the parameters that measure width. For features beyond 1.8 μm, these resolution uncertainties are on the order of 1200 km s^{-1} near 3 μm, 2000 km s^{-1} near 6 μm, and 500 km s^{-1} near 12 μm. Uncertainties from the fitting were calculated using a bootstrap resampling method. Uncertainties in width parameters such as FWHM and inner-shell velocity were obtained by adding the resolution and fitting uncertainties in quadrature.

3.2. Iron-group Elements: Fe, Co, and Ni

Starting with the isolated and well-resolved [Co III] 11.89 μm line, we approximate the shape of the line profile by the sum of two Gaussians with FWHM = 5400 $\pm$ 1900 km s^{-1} and kinematic offset $v_{offset} = 4600 \pm 2300$ km s^{-1}, and FWHM = 8000 $\pm$ 2200 km s^{-1} and kinematic offset $v_{offset} = 1400 \pm 1800$ km s^{-1}. As shown in Figure 3, the [Fe II] 1.26 μm line has a shape very similar (taking into account the neighboring [Fe II] lines that create its red tail) to that of [Co III] 11.89 μm, so we fit all the [Fe II] lines across 1.20–1.83 μm with a sum of two Gaussians and obtain a similar, but slightly more peaked, profile for [Fe II] with FWHM = 4700 $\pm$ 1200 km s^{-1} and kinematic offset $v_{offset} = 3800 \pm 500$ km s^{-1}, and FWHM = 7400 $\pm$ 2100 km s^{-1} and kinematic offset $v_{offset} = -600 \pm 1300$ km s^{-1} (see Figure 4 for a visualization of a double-Gaussian profile).

A possible explanation for why Fe and Co do not exhibit exactly the same profiles is that while Co mostly traces the original ^{56}Ni profile, Fe is more widely distributed because it is partially primordial. In the regions dominated by the IMEs and O + Ne, Fe may be a significant coolant since primordial Fe is ~400 times more abundant than Co. Additionally, or alternatively, the Co may be less sharply peaked as this may be the region corresponding to partial burning in quasi nuclear statistical equilibrium (DerKacy et al. 2023).

Although the MIR isolated Ni lines are weak and low resolution, [Ni II], [Ni III], and [Ni IV] all exhibit a very similar line-profile shapes. Likewise, the [Co II] lines have a similar shape as [Co III] and the [Fe III] lines have a similar shape as [Fe II]. Thus, to reduce degeneracy and make fitting many ions (and therefore parameters) more tractable, we use the same profile-shape parameters (excluding amplitude) for all ionization states of the same element for Co, Fe, and Ni. We find that the Ni lines are slightly better fit by the Fe parameters than by Co, so we use the same profile-shape parameters as [Fe II] for all Ni lines. In principle, we would not necessarily expect different ionization states of the same element to arise from the same emitting regions; however, Figure 4 shows that our constraints on these profile fits can reproduce the emission features very well from the optical through the MIR. This suggests that there is not significant ionization stratification in the IGEs (i.e., emission from different ionization states is coming from similar ejecta regions). Furthermore, the IGE lines all peak with a redshift ~ 3500 km s^{-1}; the consistency of these profiles indicates that the IGEs are present in roughly the same ejecta regions.
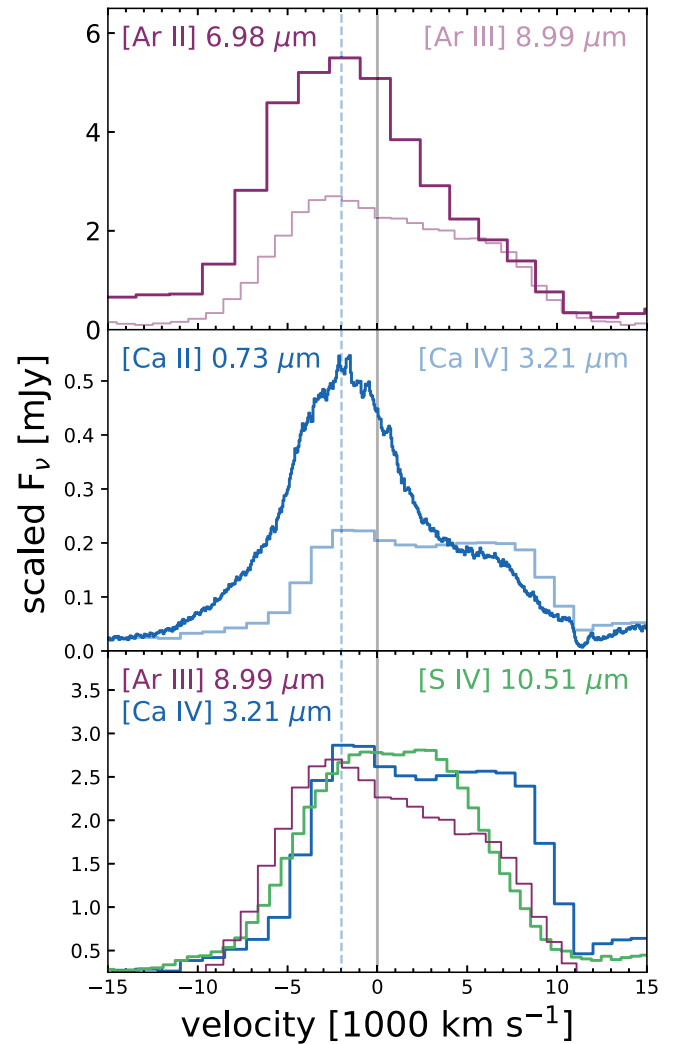

Figure 5. Comparison of the [Ar II] 6.98 μm and [Ar III] 8.99 μm lines, as well as the optical [Ca II] $\lambda\lambda$7291, 7324 and NIR [Ca IV] 3.21 μm lines. The lower-ionization states show a more prominent blueshifted peak (vertical dashed blue line), while the higher-ionization states exhibit more of an asymmetric, slanted flat-topped shape. The bottom panel shows a comparison between the high-ionization states of the IMEs. The [S IV] 10.51 μm appears more flat-topped owing to the neighboring [Co II] 10.52 μm line, which peaks toward the red. The different profile shapes between ionization states imply ionization stratification.

3.3. Intermediate-mass Elements: S, Ar, and Ca

The emission from IMEs in SN 2022pul is very strong and displays more line-profile variation than the IGEs. Despite the variation, the IME emission-line profiles share similar shapes and all exhibit a blueshifted peak at ~−2000 km s^{-1}, the opposite direction as the IGEs. They also exhibit ionization stratification, shown in Figure 5. The higher-ionization states of [S IV], [Ar III], and [Ca IV] all have a generally asymmetric boxy shape, whereas the lower-ionization [Ar II] and [Ca II] appear to have an additional blueshifted, Gaussian-like component. We choose to fit the Ca II and Ar II features with the sum of a Gaussian and a slanted flat-top profile. Physically this could mean that the central, denser regions of the ejecta have lower overall ionization, requiring this additional Gaussian component (see Figure 6 for a visualization of an asymmetric shell and an additional Gaussian component profile).
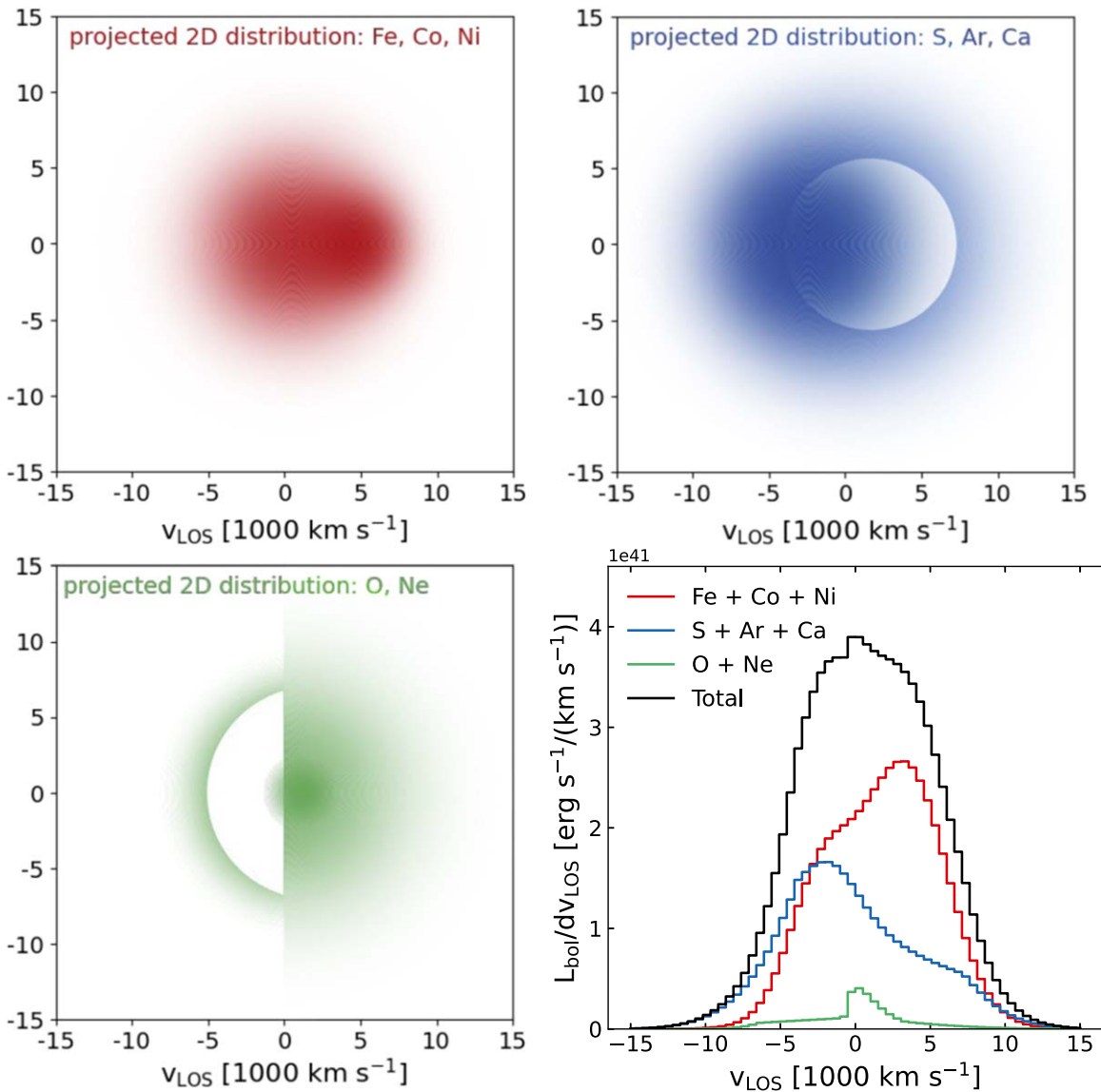
Figure 6. Top left, top right, and bottom left: cartoon projected 2D geometric interpretations of the IGE, IME, and O + Ne line profiles, respectively, assuming axial symmetry. Bottom right: bolometric luminosity per projected velocity bin (500 km s^{-1}) along the line of sight for the IGEs (Fe, Co, and Ni), the IMEs (S, Ar, and Ca), and O + Ne. There are clear differences in the overall line profiles from each element group, indicating distinct geometric distributions of material. This bolometric luminosity plot, derived from the spectral line profiles of the data (independent of the cartoon models), gives the true relative contributions of the different element groups without suggesting microscopic mixing.

The right panel of Figure 4 shows our best-fit line profiles for the IMEs. The [Ar III] 8.99 μm line is isolated and exhibits a clear slanted, flat-topped shape with Gaussian wings. This flat-topped Gaussian profile can arise from a thick shell of [Ar III] emission, where one side of the shell is thicker than the other, causing the slant. The viewing angle of this asymmetric shell also contributes to the observed slant (DerKacy et al. 2023). The parameters for our [Ar III] 8.99 μm fit are FWHM = 10,300 $\pm$ 1100 km s^{-1} for the Gaussian wings, overall kinematic offset $v_{offset} = 700 \pm 300$ km s^{-1}, inner-shell velocity $v_{min} = 5400 \pm 900$ km s^{-1}, and offset of the shell thickness $v_{offset,\ shell} = -1000 \pm 200$ km s^{-1}.

As described above, we fix the fit parameters (excluding amplitude) for [Co II] 10.52 μm and [Ni III] 11.00 μm, and then we fit the remaining contribution to the feature at 10.5 μm as

the [S IV] 10.51 μm line. This yields a slanted boxy profile with Gaussian wings for [S IV], with a similar width and slope as [Ar III], but a narrower inner-shell radius. Its parameters are FWHM = 8200 $\pm$ 800 km s^{-1}, kinematic offset $v_{offset} = -1000 \pm 200$ km s^{-1}, inner-shell velocity $v_{min} = 2500 \pm 700$ km s^{-1}, and offset of the shell thickness $v_{offset,\ shell} = -1300 \pm 300$ km s^{-1}.

When we assume the peak of the [Co II] 10.52 μm line is redshifted (like all the relatively isolated IGE ions consistently display), we recover a blueshifted peak for [S IV] that agrees with the other IMEs. Because the IGEs are redshifted and the IMEs are blueshifted, we are able to distinguish the contributions to the 10.5 μm feature from both [Co II] 10.52 μm and [S IV] 10.51 μm. We do not attribute the full flat-topped, boxy shape of the feature at 10.5 μm to [S IV] 10.51 μm alone

because the neighboring [Co III] 11.89 μm line is quite strong, and SN 2022pul has a low mean ionization state, so we do not expect the contribution from [Co II] 10.52 μm to be negligible.

The [Ca IV] 3.21 μm line can also be fit reasonably well by an asymmetric boxy profile with slightly larger width than [Ar III] and shallower slope. Its parameters are FWHM = 7500 ± 1300 km s^{-1}, kinematic offset $v_{offset} = -2400 \pm 200$ km s^{-1}, inner-shell velocity $v_{min} = 5900 \pm 1100$ km s^{-1}, and offset of the shell thickness $v_{offset, shell} = -200 \pm 200$ km s^{-1}. Simultaneously fitting the nearby [Fe III] around 2.9 μm, we constrain the contribution to the [Ca IV] profile from [Fe III] 3.23 μm to be very minimal. Thus, most of the flux in this feature is from [Ca IV], though [Ni I] 3.12 μm may contribute to the narrow peak on the blue side of the [Ca IV] emission.

[Ar II] 6.98 μm and [Ca II] $\lambda\lambda$7291, 7324 show similar line profiles (see Figure 3), and the [Ca II] line is helpful for interpreting the general shape of the low-resolution [Ar II] line. Figure 5 shows that the [Ar III] 8.99 μm line shape fits nicely with the [Ar II] 6.98 μm line if a blueshifted component is added. Thus, we fit [Ar II] 6.98 μm by summing a Gaussian with a forced contribution from the shape of [Ar III]. Since [Ca II] shares a similar shape to [Ar II], with a Gaussian-like peak and a somewhat boxy red wing, we also fit it with the sum of a Gaussian and a forced contribution from the shape of the [Ar III]. For [Ar II] the additional Gaussian component has FWHM = 9300 ± 1700 km s^{-1} and a kinematic offset $v_{offset} = -2300 \pm 100$ km s^{-1} and for [Ca II] the additional Gaussian component has FWHM = 4700 ± 200 km s^{-1} and a kinematic offset $v_{offset} = -1500 \pm 100$ km s^{-1}. Because the optical 0.73 μm region is complex with contribution from many lines, including [Fe II], [Ni II], and [Ar III], we fit all of these additional lines simultaneously with the [Ca II] doublet and find their contribution to be relatively small. While we cannot definitively rule out other line-profile shapes for [Ca II] and [Ar II], it is clear that they exhibit an additional blueshifted peak of emission not seen in the higher IME ionization states.

The shapes of these IME line profiles and their ionization stratification point to the presence of broad, asymmetric shells of higher-ionization IME material, and a somewhat narrower, blueshifted region of lower-ionization IME material.

3.4. O and Ne

In the center-bottom panel of Figure 4, we display our best-fit line profiles for [O I] and [Ne II]. The [O I] $\lambda\lambda$6300, 6364 feature is remarkably narrow (FWHM = 2500 ± 100 km s^{-1}), allowing us to resolve emission from both components of the doublet. We do not detect emission from either [O II] λ3727 or [O III] $\lambda\lambda$4959, 5007; however, this region of the spectrum is dominated by low-ionization-state IGEs, complicating the interpretation of the blended features. The [O I] emission is best modeled by a single skewed Gaussian velocity component. Similar skewed (or "sawtoothed") emission has been observed in the [Fe II] and [Ca II] features of other 03fg-like SNe Ia (Taubenberger 2017; Siebert et al. 2023, 2024). This asymmetry could potentially be explained by either an intrinsically asymmetric ejecta distribution or dust extinction from within the SN ejecta.

If a large amount of dust were present in the ejecta, assuming it did not render the [O I] emission invisible, one would expect the redshifted emission to be more heavily extinguished than the blueshifted emission. This would lead to an emission profile whose total offset is preferentially blueshifted, appears steeper

on the blueshifted side, and is more shallow sloped on the redshifted side (Jerkstrand 2017). There is some evidence that the [Ca II] features of 03fg-like SNe are preferentially blueshifted (Siebert et al. 2024); however, one would expect more dust attenuation at shorter wavelengths. Furthermore, the [O I] in SN 2022pul is redshifted by 260 ± 10 km s^{-1}, so the systemic velocity of the ejecta (and dust) would need to be redshifted if dust extinction were the cause of the asymmetric line profile. This could be the case; however, we do not observe evidence for such a systemic shift in the other nebular features, and therefore favor an asymmetric ejecta distribution.

The [Ne II] 12.81 μm emission has a unique profile compared to the other elements. There is a narrow peak close to $\sim$0 km s^{-1}, indicating that it is present in the central regions of the ejecta along with [O I]. However, most of the [Ne II] emission is likely not coincident with the [O I] owing to its much larger ionization potential. The overall broad [Ne II] line suggests that it forms at large velocities similar to the IMEs and IGEs. We model the broad component of the [Ne II] line profile with a broad Gaussian on the red side (FWHM = 10000 ± 500 km s^{-1}), and an asymmetric, slanted, flat-top on the blue side (FWHM = 7200 ± 600 km s^{-1}, kinematic offset $v_{offset} = 1400 \pm 200$ km s^{-1}, inner-shell velocity $v_{min} = 7000 \pm 500$ km s^{-1}, and offset of the shell thickness $v_{offset, shell} = 800 \pm 100$ km s^{-1}). The one-sided asymmetric slant is tilted in the opposite direction as the tilt of the IMEs, and could arise from a half-shell or some type of missing bubble of [Ne II] on the blueshifted side (see Figure 4 for visualization of this profile). The overall shape of this profile does not appear as blueshifted as the other IMEs, and the differing locations of missing emission indicate that the distributions of Ne and the IMEs are distinctly different.

The highly asymmetric [Ne II] line shares some of the same projected velocities, but it cannot coexist with the IMEs and IGEs, indicating large-scale composition asymmetry. Additionally, the small-scale structure seen throughout the [Ne II] profile may be caused by the presence of a large number of randomly distributed blobs (e.g., see Jerkstrand 2017, Figure 3); alternatively, it may be due to higher noise levels at the longest MIRI/LRS wavelengths. Other higher-resolution optical and NIR emission lines, including the [O I] $\lambda\lambda$6300, 6364 feature, do not show convincing evidence for small structure in the line profiles that would suggest clumping on large scales (see Section 4). In Section 5, we discuss the detection of [Ne II] 12.81 μm in relation to predictions from WD–WD violent merger models.

3.5. Geometric Interpretation: Distinct Ejecta Distributions

The difference in line profiles suggests differences in the geometric distributions of material in the ejecta. In order to compare more easily between the bulk emission coming from each group of elements (IGEs: Fe, Co, and Ni; IMEs: S, Ar, Ca; and O + Ne), rather than from particular elements and ions, we sum all of the line profiles across our full wavelength range within these three groups in velocity space and calculate the bolometric luminosity along the line of sight in bins of 500 km s^{-1} ($d\nu\, L_{bol}$). Each velocity bin represents a slab of emission on the plane of the sky, giving a 2D-projected spatial distribution of the elements. Shown in the bottom right panel of Figure 6, the summed profiles of the IGEs, IMEs, and O + Ne are close to those of the individual profiles, but they erase the small variations seen from profile to profile.
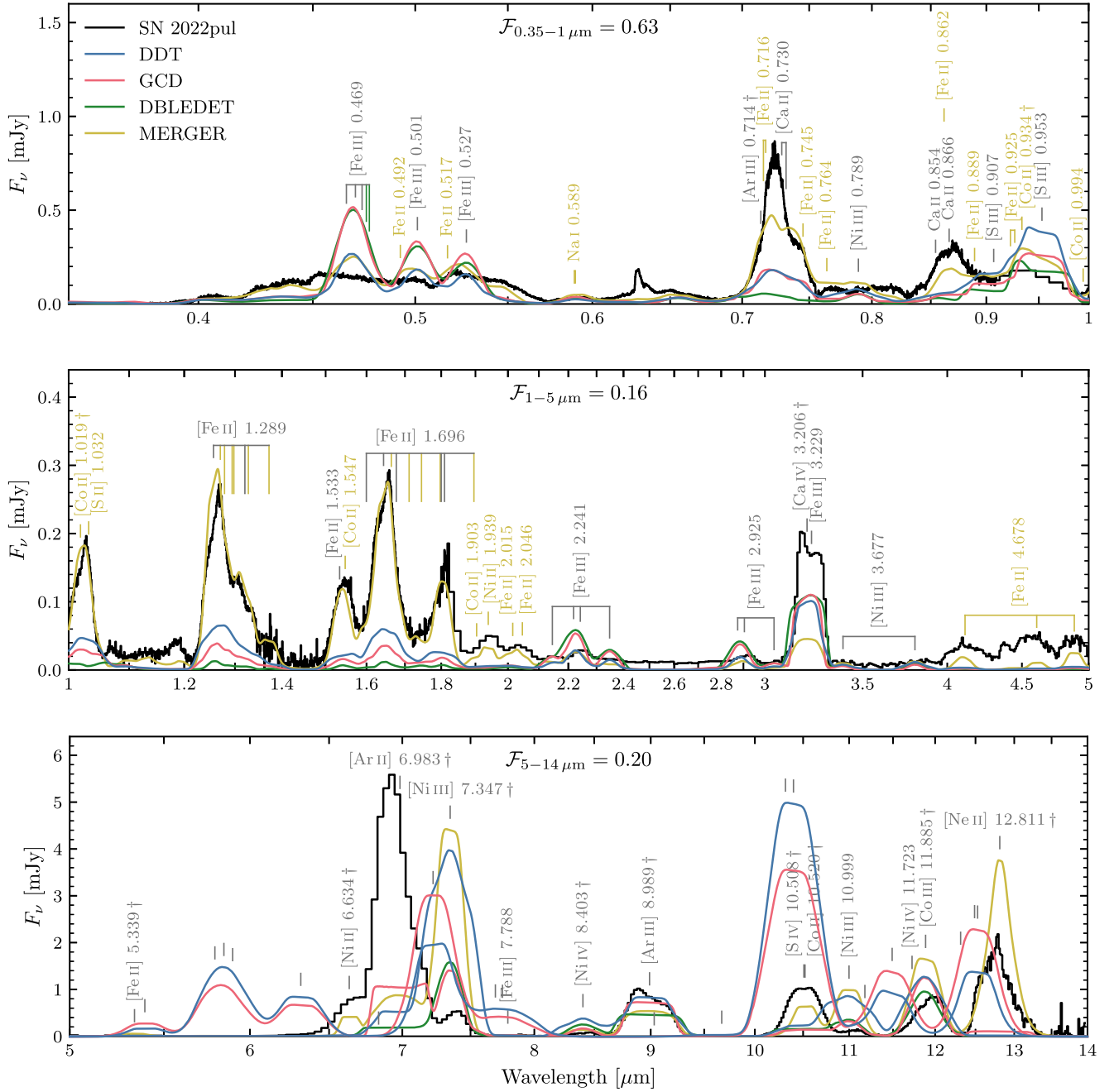
Figure 7. Spectra of our reference model set at 338 days postexplosion compared to the dust- and MIR-continuum-subtracted spectrum of SN 2022pul over the wavelength ranges (from top to bottom): optical (0.35–1 μm), NIR (1–5 μm), lower MIR (5–14 μm), and upper MIR (14–28 μm). The SN 2022pul spectrum has been corrected for redshift and Milky Way extinction. The synthetic fluxes correspond to the assumed distance to SN 2022pul of 16 Mpc; they have not been rescaled or normalized in any way. The $F_{X-Y\,\mu m}$ label gives the fraction of the total optical to MIR flux (0.35–14 μm) for SN 2022pul emitted within the wavelength range of each plot. We include line identifications based on their Sobolev equivalent widths, as in Blondin et al. (2023; see Table 1). Transitions connected to the ground state are marked with a "†" symbol. For consecutive lines within a multiplet (connected by a horizontal line), we give the *gf*-weighted mean wavelength of the transitions.

Using the geometric interpretations of the line-profile components that we adopt in our fits, we construct cartoons for the projected 2D distribution of our three element groups to aid visualization of the distinct regions (see Figure 6). Assuming spherical symmetry, Gaussian emission distributions produce Gaussian line profiles, and slanted flat-topped (or boxy) profiles result from asymmetric shells of emission. We assume spherical symmetry for the individual components of each profile (resulting in overall axial symmetry for the 2D-projected distributions) and stick to combinations of these two

basic line-profile shapes, so our cartoons are oversimplifications. The real ejecta are probably asymmetric and complex, potentially including bubbles, mushroom shapes, and clumps. Pakmor et al. (2012) show the distribution of elements in their WD violent merger hydrodynamical simulation in their Figure 2. Interestingly, our cartoons bear some similarities to these physically realistic distributions.

We stress that these cartoons are not to be taken literally and that they are 2D projections. Overlap in line-of-sight velocity ($v_{\rm LOS}$) between the element groups does not necessarily imply
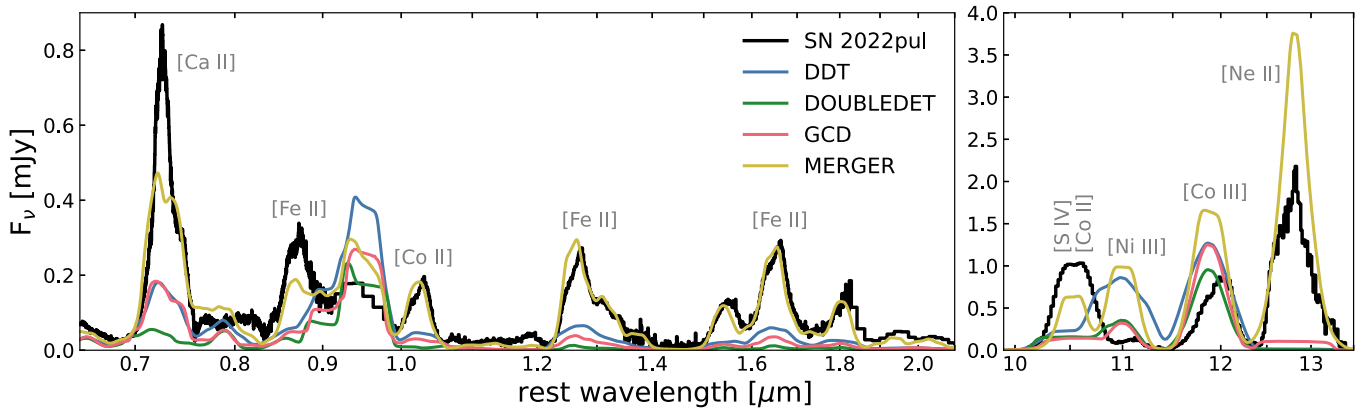
Figure 8. Similar to Figure 7 but highlighting the 0.7–2 μm and 10–14 μm regions where the models diverge substantially. The MERGER model matches the observed spectrum of SN 2022pul best, notably producing stronger [Ca II] near 0.73 μm, capturing the NIR [Fe II] lines extremely well, and predicting the strong observed [Ne II] 12.81 μm line that is not seen in the other models. However, there are also deficiencies to the MERGER model, such as the strength of the Ni lines being overpredicted (e.g., [Ni III] 11.00 μm).

that they are physically colocated in 3D space. Specifically, all of our distributions show emission at $v_{LOS} = 0$ km s^{-1}; however, this is a projection effect because, from theoretical models, there should be very little to no IGEs or IMEs in the most central regions where the [O I] emission is located.

3.6. Nickel-56 Mass

At the late phase of SN 2022pul (338 days postexplosion), the ^{56}Ni (half-life $\sim$ 6 days) has long since decayed away and the energy deposition that continues to power the spectral emission lines comes from the radioactive decay of ^{56}Co (half-life $\sim$ 77 days). Locally deposited gamma-rays and positrons from the decay can be absorbed by the IGEs and some IMEs in the IGE-rich regions, while the IMEs and unburned elements outside this region can absorb nonlocally deposited gamma-rays and secondary, low-energy photons. Thus, to estimate the initial mass of ^{56}Ni synthesized in the explosion, we account for the total flux by integrating the spectrum ($F = \int F_\nu \, d\nu$) in the range 0.4–14 μm. We then estimate the luminosity from the emission lines by correcting the flux to a distance of 16 Mpc (see Paper I, Siebert et al. 2024, for a discussion of the distance to SN 2022pul). In the low-density nebular phase, however, most of the energy escapes. To account for this, we divide by the fraction of the total decay energy that is absorbed by the ejecta from the MERGER model (Blondin et al. 2023; and described further in Section 4), which has a value $E_{absorbed}/E_{total} = 0.055$.

Using the uncertainty in the distance (16 ± 2 Mpc) as the dominant source of uncertainty in our calculation, we estimate a bolometric luminosity (i.e., deposited ^{56}Co decay power) at 338 days postexplosion of $4.6 \pm 1.2 \times 10^{41}$ erg s^{-1}, which corresponds to a mass of synthesized ^{56}Ni of 0.66 ± 0.17 $M_\odot$ (see the equations from Nadyozhin 1994; Branch & Wheeler 2017, Section 5.4). This estimate may also suffer from uncertainties in reddening, absolute-flux calibration, gamma-ray escape fraction, and the assumption of spherical symmetry, but these uncertainties should be smaller than the 25% uncertainty introduced by the distance. Our estimated ^{56}Ni mass is in rough agreement with the 0.6 $M_\odot$ of ^{56}Ni produced in the violent merger simulation of Pakmor et al. (2012) and the calculated ^{56}Ni masses for SN 2011fe, the canonical normal SN Ia (Bora et al. 2022, and references therein).

4. White Dwarf–White Dwarf Violent Merger Model

Blondin et al. (2023) presented nebular-phase spectra from four different SN Ia explosion models at 270 days postexplosion: a M_{Ch} delayed-detonation model (Seitenzahl et al. 2013), a M_{Ch} pulsationally assisted gravitationally confined detonation model (GCD; Lach et al. 2022), a sub-M_{Ch} double-detonation (Gronow et al. 2021), and a violent merger of two sub-M_{Ch} WDs ($0.9 + 1.1$ $M_\odot$; MERGER; Pakmor et al. 2012), which they compared to a spectrum of SN 2021aefx covering the wavelength range 0.3–14 μm from Kwok et al. (2023). These model spectra are generated assuming spherical symmetry, so the line-profile shapes do not reflect ejecta asymmetries that might be seen in 2D models. Only the MERGER model displayed a strong, centrally peaked line due to [Ne II] 12.81 μm, resulting from the presence of Ne in the innermost ejecta layers of this model. None of the other models considered by Blondin et al. (2023) presented such a strong [Ne II] feature, and only the GCD model displayed a weak flat-topped line, whose intensity at the line center was a factor $\sim$ 3 smaller than observed in SN 2021aefx. Only by artificially setting a minimum Ne mass fraction of 10^{-2} in the inner ejecta of the GCD model were they able to match the peak intensity and profile shape of the potential weak [Ne II] line in SN 2021aefx. Future analysis of subsequent observations of SN 2021aefx should clarify whether [Ne II] 12.81 μm is actually present in SN 2021aefx (C. Ashall et al. 2024, in preparation).

The violent merger model naturally predicts the presence of Ne in the inner ejecta layers, which is associated with the delayed and incomplete burning of the lower-mass secondary WD. Moreover, the higher density in layers $\lesssim$10,000 km s^{-1} enhances the recombination rate there, which in turn results in a lower mean ionization state compared to the other explosion models. For comparing to the nebular spectrum of SN 2022pul, we recomputed the four models studied by Blondin et al. (2023) at a later time of 338 days postexplosion, using the same numerical setup. The full optical through MIR comparison of these models to the observed spectrum is displayed in Figure 7 and highlights of the results are shown in Figure 8.

Given the limited range of models from very different origins, we compare qualitatively rather than quantitatively. Of the four models, we favor the MERGER model for several reasons: (1) it predicts a lower overall ionization state that is in good agreement with the NIR [Fe II] lines; (2) it predicts
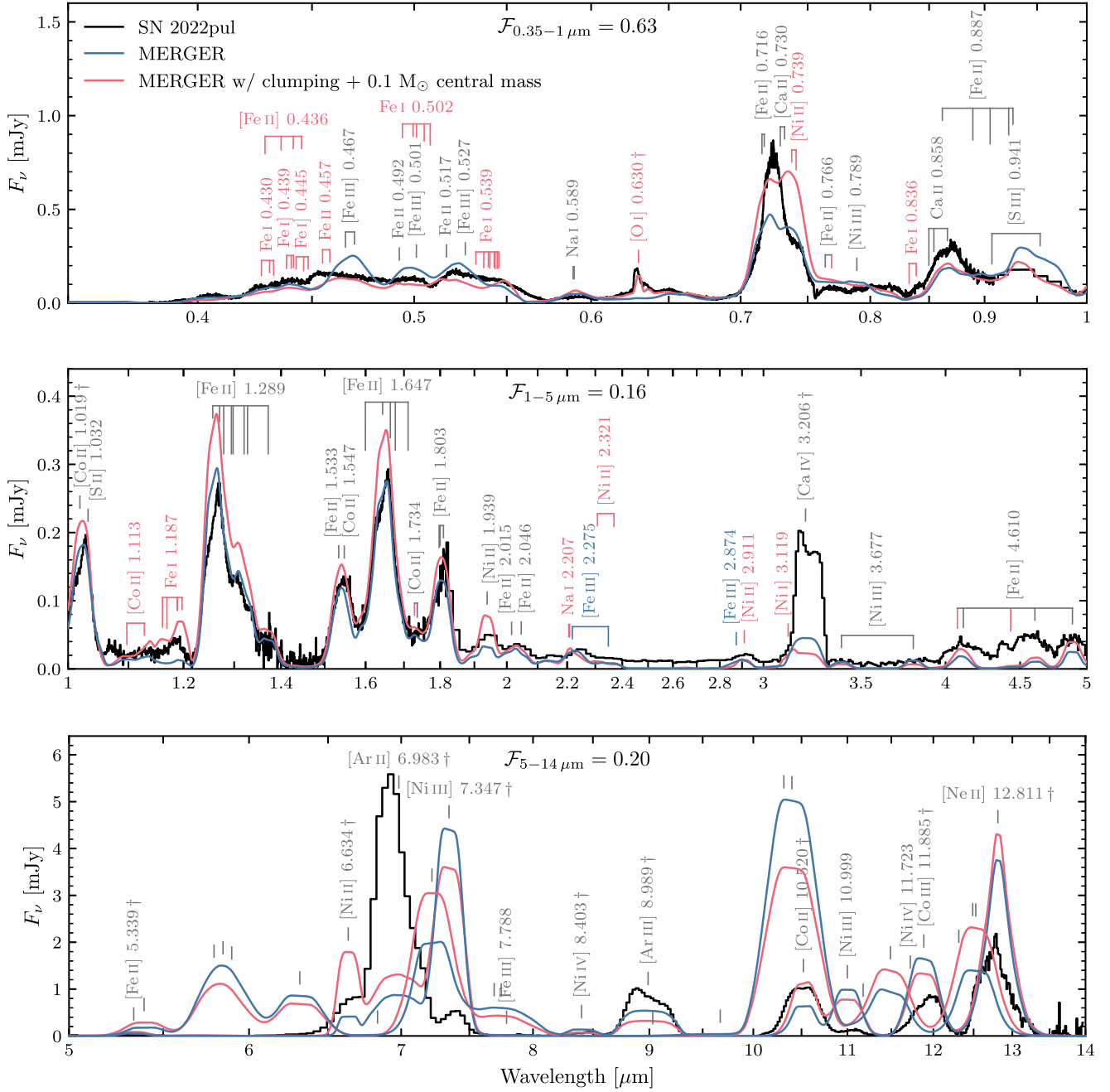
Figure 9. Similar to Figure 7 but for our reference (blue) and modified (red) merger models.

rounded IME emission profiles, indicating that the IMEs are centrally located, whereas the other models predict very flat profiles for all ionization species, indicating that the IMEs are absent in the center; and (3) it is the only model consistent with the strong, centrally peaked [Ne II] 12.81 μm line.

The lower ionization results in a better match to the numerous [Fe II] features in the 1–2 μm range, yet the optical [Fe III] complex around 0.5 μm is still too strong compared to SN 2022pul, as is the [Ni III] 7.35 μm line. This suggests the ionization in SN 2022pul is even lower than predicted in the MERGER model. We consider clumping to be a viable mechanism to reduce the ionization state in this model further. Using the same approach as Blondin et al. (2023), we recomputed a clumped version of the MERGER model with a volume-filling factor $f = 0.5$ (i.e., resulting in a factor of 2

increase in the density of the clumps). Clumpy ejecta can leave an impact on emission lines (e.g., nebular spectra of the Type Ib SN 1985F and of the Type IIb SN 1993J; Filippenko & Sargent 1989; Filippenko et al. 1994; Houck & Fransson 1996), but these would need to be large clumps with a large density contrast (i.e., dense shells in 1D or large clumps in 3D), whose physical origin in SN Ia ejecta is unclear. In our modeling approach the clumps are significantly smaller than the photon mean free path, so we see a global impact on the ionization state (through enhanced recombination) but no small structure in the line profiles.

As seen in Figure 9, this clumped model is able to match the flux level in the [Fe III]-dominated complex better, while maintaining a satisfactory match out to ~3 μm. The lower ionization also results in a stronger [Ar II] 6.98 μm line and a
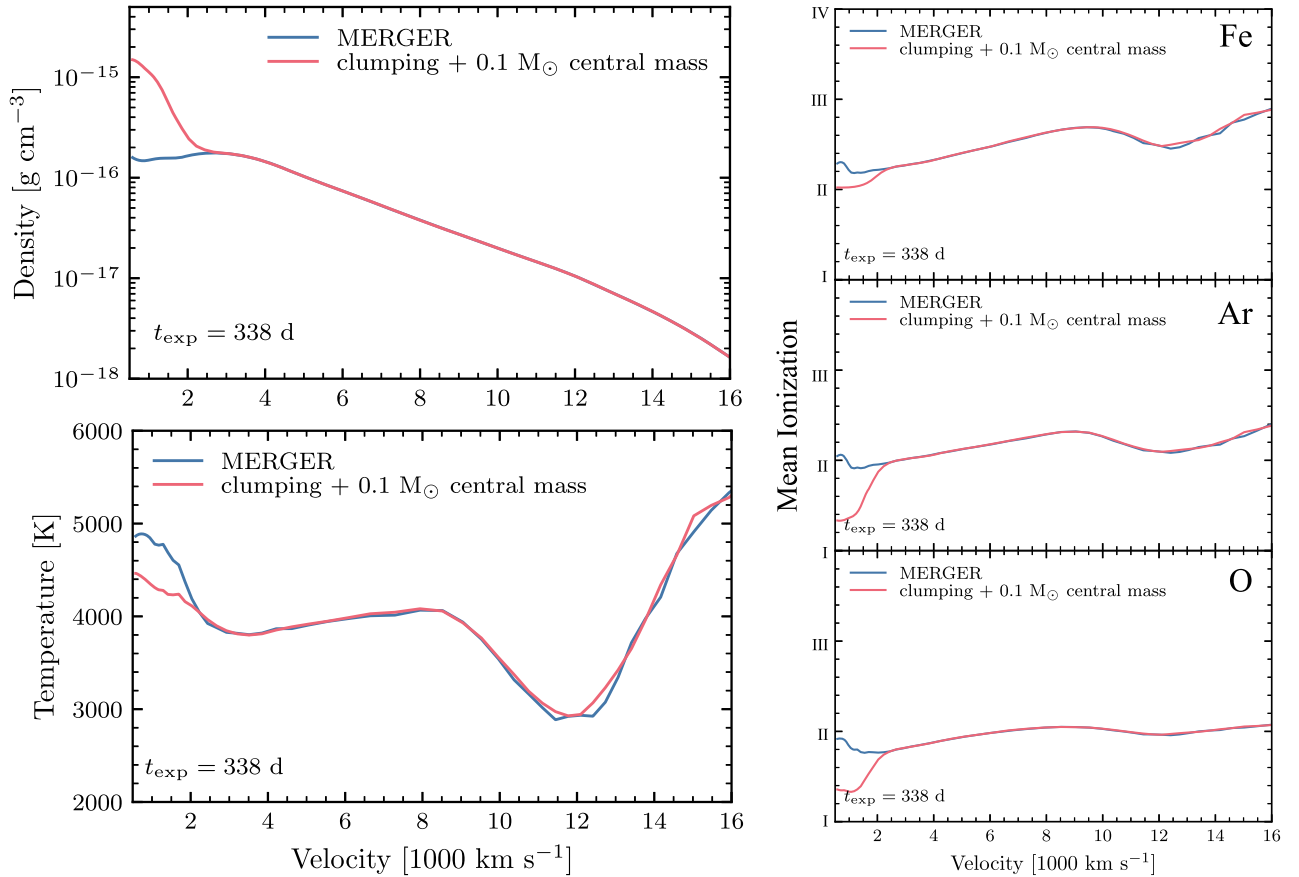
Figure 10. Top left: density profiles at 338 days for the MERGER model and our modified merger model with clumping and 0.1 $M_\odot$ of mass added to the central ($\lesssim 2000$ km s^{-1}) region. Bottom left: temperature profiles. Top right: mean Fe ionization profiles. The mean ionization is defined as $\Sigma_i i n^{i+}/\Sigma_i n^{i+}$, where n^{i+} is the number density of ionization stage i for Fe, such that a mean ionization ~ 2 indicates that Fe^{2+} is the dominant stage. Middle right: mean Ni ionization profiles. Bottom right: mean O ionization profiles.

weaker [Ni III] 7.35 μm line. However, it also results in an even weaker [Ca IV] 3.12 μm line compared to SN 2022pul. The same is true of [Ar III] 8.99 μm. Moreover, the [Ni II] 6.63 μm and [Ni III] 7.35 and 11.00 μm lines remain too strong. This suggests that the clumping is not uniform, affecting some regions more strongly than others.

The mismatch in lines from specific elements over several ionization stages suggests that abundance also plays a role. Here, a lower abundance of stable Ni and a higher abundance of Ar/Ca could help resolve some of these discrepancies. In particular, a lower abundance of stable Ni (~ 0.03 $M_\odot$ in this MERGER model) seems warranted to reproduce the lines of Ni II and Ni III in the observed spectrum. Pakmor et al. (2013) show in their helium-ignited violent merger of a system of $0.9 + 0.76$ $M_\odot$ WDs that the central density and the Ar/Ca abundance is higher in the innermost layers, while the stable Ni abundance is lower and more centrally concentrated than the merger from Pakmor et al. (2012), upon which the MERGER model is based. Additionally, the amount of stable Ni in the merger model from Pakmor et al. (2012) scales with the metallicity of the progenitor system ($Z = Z_\odot$ in the model), so a lower stable Ni abundance may imply the progenitor system had subsolar metallicity. There may be a variety of inner-ejecta properties that could be produced through violent merger scenarios that would better match the observations of SN 2022pul.

Despite the lower ionization of the clumped MERGER model, the [O I] $\lambda\lambda 6300$, 6364 emission remains very weak compared with SN 2022pul. This is not related to an abundance issue, since oxygen completely dominates the ejecta layers below ~ 2000 km s^{-1} in the MERGER model (mass fraction $\gtrsim 0.5$). Radial compression does not change the optical depth, so the mass of inner material must be increased to boost the amount of gamma-ray energy intercepted by the inner, O-rich ejecta layers. We were able to match the intensity and width of the narrow [O I] feature seen in SN 2022pul by artificially increasing the density below ~ 2000 km s^{-1}. In practice we followed the procedure from Dessart et al. (2020) and added a Gaussian component to the original density profile centered on the inner boundary of our spatial grid ($v_{\rm min} \approx 580$ km s^{-1}) with a width $\sigma \approx 600$ km s^{-1}, resulting in an additional 0.1 $M_\odot$ in these layers ($\sim 50\%$ of which is O). The original mass of O (0.53 $M_\odot$) was all located in the inner ejecta and the total ejecta mass in the model is increased through this modification. The fractional O abundance in the innermost region is not particularly important, as long as [O I] $\lambda\lambda 6300$, 6364 remains the dominant coolant.

As seen from Figure 9, the narrow [O I] feature is well reproduced, while the rest of the spectrum remains largely unchanged compared to the original model. The physical origin of such an increase in density in the inner ejecta is likely the result of a higher-mass secondary WD (e.g., Pakmor et al. 2013). Other contributing effects could be how completely the

Table 1
Lines in the Wavelength Range 0.35–14 μm in Our Modified Merger Model (MERGER with Clumping and 0.1 $M_\odot$ Central Mass) at 338 Days Postexplosion Whose Absolute Sobolev Equivalent Width Exceeds 5% of the Largest Absolute Equivalent Width in the Wavelength Range 0.35–1 μm

λ_{air} (μm)	Ion	λ_{air} (μm)	Ion	λ_{air} (μm)	Ion	λ_{air} (μm)	Ion	λ_{air} (μm)	Ion	λ_{air} (μm)	Ion	λ_{air} (μm)	Ion
0.427	Fe I [a]	0.501	[Fe III] [i]	0.717	[Fe II] [m]	0.923	[Fe II] [t]	1.321	[Fe II] [y]	1.954	[Fe II] [aa]	5.672	[Fe II] [ah]
0.429 †	[Fe II] [b]	0.501	Fe I [h]	0.729 †	[Ca II] [n]	0.927	[Fe II] [t]	1.328	[Fe II] [y]	1.967	[Fe II] [ab]	5.703	[Co II] [ai]
0.431	Fe I [a]	0.502	Fe II [g]	0.732 †	[Ca II] [n]	0.934 †	[Co II] [v]	1.372	[Fe II] [y]	2.007	[Fe II] [ad]	6.212	[Co II] [ai]
0.433	Fe I [a]	0.505	Fe I [h]	0.738 †	[Ni II] [o]	0.934	[Co II] [w]	1.497	[Co II] [z]	2.015	[Fe II] [ae]	6.634 †	[Ni II]
0.436	[Fe II] [b]	0.508	Fe I [h]	0.739	[Fe II][m]	0.953	[S III] [u]	1.533	[Fe II] [aa]	2.046	[Fe II] [ad]	6.719	[Fe II] [ah]
0.438 †	Fe I] [c]	0.516	[Fe II]	0.741	[Ni II] [o]	0.964	[Co II] [v]	1.547	[Co II] [z]	2.133	[Fe II] [ad]	6.918	[Ni II]
0.438	Fe I [d]	0.517	Fe I [j]	0.745	[Fe II] [m]	0.994	[Co II] [w]	1.599	[Fe II] [aa]	2.206	Na I [af]	6.983 †	[Ar II]
0.440	Fe I [d]	0.517	Fe II [g]	0.764	[Fe II] [p]	1.019 †	[Co II] [v]	1.626	[Co II] [z]	2.208	Na I [af]	7.347 †	[Ni III] [aj]
0.441	[Fe II] [b]	0.517	Fe I	0.769	[Fe II] [p]	1.025	[Co II][v]	1.634	[Co II] [z]	2.224	[Fe II] [ae]	7.505 †	[Ni I] [ak]
0.442	Fe I] [d]	0.523	Fe I [j]	0.789	[Ni III] [q]	1.028	[Co II] [v]	1.644	[Fe II] [aa]	2.244	[Fe II] [ad]	7.788	[Fe III]
0.442 †	[Fe II]	0.527	Fe I [k]	0.833	Fe I [r]	1.032	[S II]	1.664	[Fe II] [aa]	2.308	[Ni II] [ac]	8.403 †	[Ni IV] [al]
0.443	Fe I] [c]	0.527	[Fe III] [i]	0.839	Fe I [r]	1.097	[Co II] [v]	1.677	[Fe II] [aa]	2.369	[Ni II] [ac]	8.989 †	[Ar III]
0.445	[Fe II] [b]	0.533	Fe I [k]	0.850	Ca II [s]	1.128	[Co II] [v]	1.711	[Fe II][aa]	2.911	[Ni II] [ac]	10.508 †	[S IV]
0.446	Fe I] [c]	0.537	Fe I [k]	0.850	[Ni III] [q]	1.161	Fe I [x]	1.728	[Co II] [z]	3.119	[Ni I]	10.520 †	[Co II] [v]
0.448	Fe I] [c]	0.540	Fe I [k]	0.854	Ca II [s]	1.169	Fe I [x]	1.736	[Co II] [z]	3.206 †	[Ca IV]	10.679	[Ni II] [am]
0.455	Fe II [e]	0.541	Fe I [k]	0.862	[Fe II] [t]	1.188	Fe I [x]	1.745	[Fe II] [aa]	3.393	[Ni III] [ag]	10.999	[Ni III] [aj]
0.458	Fe II [e]	0.543	Fe I [k]	0.866	Fe I [r]	1.188	Fe I [x]	1.748	[Fe II] [ab]	3.801	[Ni III] [ag]	11.164	[Co II] [v]
0.466 †	[Fe III] [f]	0.543	Fe I [k]	0.866	Ca II [s]	1.197	Fe I [x]	1.797	[Fe II] [aa]	4.075	[Fe II] [ah]	11.304	[Ni I] [ak]
0.470	[Fe III] [f]	0.545	Fe I [k]	0.869	Fe I [r]	1.249	[Fe II] [y]	1.800	[Fe II] [aa]	4.114 †	[Fe II] [ah]	11.723	[Ni IV] [al]
0.481	[Fe II]	0.546	Fe I [k]	0.882	Fe I [r]	1.257 †	[Fe II] [y]	1.809	[Fe II] [aa]	4.434	[Fe II] [ah]	11.885 †	[Co III]
0.489	[Fe II]	0.589 †	Na I [l]	0.889	[Fe II] [t]	1.270	[Fe II] [y]	1.811	[Fe II] [ab]	4.606	[Fe II] [ah]	11.998	[Ni I]
0.492	Fe II [g]	0.590 †	Na I [l]	0.903	[Fe II] [t]	1.279	[Fe II] [y]	1.895	[Fe II] [aa]	4.888	[Fe II] [ah]	12.252 †	[Co I]
0.494	Fe I [h]	0.630 †	[O I]	0.905	[Fe II] [t]	1.294	[Fe II] [y]	1.903	[Co II] [z]	5.061	[Fe II] [ah]	12.725	[Ni II] [am]
0.499	Fe I [h]	0.716	[Fe II] [m]	0.907	[S III] [u]	1.298	[Fe II] [y]	1.939	[Ni II] [ac]	5.339 †	[Fe II] [ah]	12.811 †	[Ne II]

Note. All wavelengths are given in air. Forbidden and semiforbidden transitions are noted using the appropriate brackets around the ion name. Wavelengths marked with a "†" symbol denote transitions connected to the ground state. Ions with the same superscript correspond to transitions within the same multiplet.

secondary WD burned, a different C/O fraction of the initial secondary WD, and compression of the innermost layers through the ^{56}Ni bubble effect (e.g., Wang 2005; Dessart et al. 2021). The changes to the ejecta properties (density, temperature, and mean ionization) in our modified merger model where clumping and a 0.1 $M_\odot$ central mass have been introduced are shown in Figure 10, and a detailed list of important emission lines in our modified merger model is given in Table 1.

While additional fine tuning of the abundances and densities of particular elements could help improve the match of any of the models, only the MERGER model can be modified to create the emergence of the narrow, central [O I] feature. This is because the other models predict essentially no O or Ne in the low-velocity central regions, while the MERGER model is actually dominated by O in the center (mass fraction ~ 0.5). Fine tuning would not produce the emergence of the central O and Ne lines in the other models because they are not dominant coolants in this region, and adding a significant central mass of O and Ne to the other models would be unphysical.

5. Discussion & Conclusions

As discussed in Paper I (Siebert et al. 2024), the detection of [O I] emission in WD SNe is exceedingly rare. SN 2022pul is now the third 03fg-like SN Ia to exhibit [O I], along with SN 2012dn (Taubenberger et al. 2019) and SN 2021zny (Dimitriadis et al. 2023). The velocity distribution of [O I] varies greatly among these SNe, while its offset is consistent with originating from the central regions of the ejecta in each case. Additionally, SN 2022pul exhibits [Ne II] peaked in the central regions and extending farther out as well. A viable

explosion model should be able to explain the presence and diversity of oxygen and neon. Both turbulent pure deflagrations (Kozma et al. 2005; Fink et al. 2014) and violent WD mergers (Pakmor et al. 2012; Kromer et al. 2013; Pakmor et al. 2013) naturally predict neon and unburned oxygen present at low velocities. A violent WD–WD merger provides an explanation for the large-scale asymmetries in the nebular emission features described in Section 3, though a turbulent deflagration could also produce asymmetries. However, a pure deflagration would produce a low-luminosity explosion with different early time spectroscopic properties, narrower nebular line profiles owing to the lower explosion energy, and weaker emission from IMEs. To check this, we ran the N100def model from Fink et al. (2014) with CMFGEN to 338 days postexplosion (not shown here) and indeed found that the MERGER model is a significantly better match to SN 2022pul for the above reasons. We therefore favor a WD merger over a pure deflagration for SN 2022pul.

The large parameter space in WD mergers could help explain the diversity of 03fg-like SNe. The variation among objects may be explained by different WD mass ratios, by the specific explosion mechanism of one or both WDs, and by observations along different lines of sight. Recent studies of 03fg-like SNe Ia have favored WD merger models occurring within a dense C/O-rich CSM (Dimitriadis et al. 2022, 2023; Siebert et al. 2023; Srivastav et al. 2023) due to rapidly evolving light-curve bumps, low-ionization nebular spectra sometimes with [O I], asymmetric and blueshifted nebular emission lines, and a larger fraction of flux in the NIR at late times than normal SNe Ia. Our observations of SN 2022pul enhance the evidence for this model for 03fg-like SNe Ia through clear dust detection,

unusual light-curve rise shape, asymmetric line profiles, strong IMEs, and central O and Ne.

In the case of SN 2022pul, we also observe distinct ejecta components with different composition offset in their bulk velocities. The secondary WD may have been partially, but not completely, disrupted when the primary WD detonated. When the burning front passes over the lower-density secondary WD material, it too can burn, synthesizing O, Ne, and the IMEs (whereas the higher-density primary WD would produce the IGEs; Pakmor 2017). The degree of ejecta asymmetry will be smaller if the secondary is more compact when the primary is burned because the ashes of the primary will be less hindered by a less disrupted secondary (Pakmor 2017).

In SN 2022pul, we observe central O and Ne, very strong emission from IMEs, and a high degree of asymmetry in the nebular line features. Furthermore, our modified merger model demonstrates that additional, concentrated central mass (0.1 $M_\odot$ at $\lesssim 2000$ km s^{-1}) is needed to reproduce the [O I] $\lambda\lambda 6300, 6364$ emission. This very centrally peaked and asymmetric [O I] emission is reminiscent of expectations of stripped material from a companion (Marietta et al. 2000; Botyánszki et al. 2018), and may indicate that the secondary WD left a significant amount of mass in the innermost region.

The central, broad Ne and strong IMEs suggest that the secondary WD material was at least partially burned (the O may be a combination of burned C and unburned O, while unburned Ne is not expected for the lower-mass secondary). A higher-mass, and therefore less disrupted, secondary WD could produce the strong IMEs and the centrally concentrated material. However, the high degree of asymmetry would suggest a more disrupted secondary, which perhaps could have left behind centrally concentrated material if it was only partially burned. This may be due in part to a viewing-angle effect where the ejecta appear more symmetric in the vertical direction, and more asymmetric in the plane of rotation (Bulla et al. 2016; Pakmor 2017). Previous measurements of 03fg-like SNe Ia have not shown strong continuum polarization (Tanaka et al. 2010; Cikota et al. 2019). More polarization data and construction of nebular spectra along different viewing angles from violent merger hydrodynamical simulations would help resolve this and improve our understanding of the 3D ejecta distributions giving rise to the asymmetric line profiles.

Another key part of understanding this progenitor scenario is its connection to the inferred presence of a dense C/O-rich CSM from the shape of the light-curve rise (Siebert et al. 2024). This requires considering scenarios where the explosion occurs either premerger during a dynamical interaction phase (commonly known as a "perimerger"), or scenarios where explosion occurs postmerger after complete disruption of the secondary WD (Guillochon et al. 2010; Pakmor et al. 2010; van Kerkwijk et al. 2010; Pakmor et al. 2012; Moll & Woosley 2013; Raskin & Kasen 2013).

In both cases, simulations of the ejecta are highly asymmetric and the synthetic light curves cover a large range in luminosity depending on viewing angle (with the highest luminosity observed along the equator). This light-curve, line-of-sight dependence might also vary over time because at early phases the interaction dominates over decay power. One beneficial consequence of the postmerger scenario is that the complete disruption of the secondary WD leads to the formation of a massive C/O-rich accretion disk. The early time light curve of SN 2022pul is consistent with ejecta interaction with this kind of CSM (Noebauer et al. 2016; Siebert et al. 2024). More work is needed to understand if a violent merger is capable of producing enough CSM at the required distance to explain this kind of interaction signature.

The large amount of CSM (0.6 $M_\odot$) adopted in the Noebauer et al. (2016) interaction model is difficult to reconcile with the central oxygen and neon seen in SN 2022pul. If this much material from the secondary WD was pulled off into an exterior spherical shell, it seems unlikely that the secondary would have enough leftover mass to create the high-density central O giving rise to the [O I] doublet and the strong emission from the IMEs. If the CSM is responsible for damping the kinetic energy of the explosion, leading to the boosted luminosity and low-velocity C II at early times, the CSM must cover a substantial fraction of the exploding system (Maeda et al. 2023). Howell et al. (2006) suggest that the extra binding energy associated with the additional mass may be enough to cause a sufficiently slow ejecta velocity. However, Raskin & Kasen (2013) find that the amount of CSM stripped from the secondary WD in their models is small, less than 0.005 $M_\odot$. If the dust emission arises from the CSM, assuming a dust-to-gas ratio of 0.01, the dust mass for SN 2022pul given by J. Johansson et al. (2024, in preparation) implies a CSM mass of 0.05–0.11 $M_\odot$, depending on composition. Further exploration is needed to address whether these lower CSM masses (or perhaps a different composition) could produce the interaction signature we observe.

Hsiao et al. (2020) present evidence supporting the "core-degenerate" model for LSQ14fmg, where a near-$M_{\rm Ch}$ WD interacts with the degenerate core of an AGB star within a common envelope stripped of its H and He through a superwind phase prior to explosion. We disfavor this scenario to explain SN 2022pul because the explosion is expected to be a spherical explosion of a single object after secular accretion. It therefore does not explain the observed central location of O and Ne or the large-scale ejecta asymmetries. It is tempting to speculate whether a modified version of this model, in which the AGB degenerate core material also undergoes thermonuclear fusion, could be developed for SN 2022pul.

Perhaps a triple system could be invoked (Kushnir et al. 2013; Grishin & Perets 2022), where one WD or star is disrupted to become the surrounding CSM and precipitates the violent merger of the remaining two WDs. Rajamuthukumar et al. (2023) found that triple systems contribute significantly to the overall SN Ia rate. Again, more detailed modeling over a wide range of possible parameters and scenarios involving WD–WD violent mergers is needed to understand better the system giving rise to this unique SN.

We summarize our main observations and discussion points below.

1. The presence of O and Ne in the central ejecta are hallmarks of the WD violent merger SN Ia model.
2. Asymmetric nebular emission-line profiles show distinct distributions of IGEs, IMEs, and O + Ne in the ejecta that can be naturally explained by the violent merger model.
3. A pure deflagration model is disfavored as it would produce lower luminosities, narrower nebular line widths, and weaker emission from IMEs than observed in SN 2022pul.
4. Especially strong emission from IMEs could come from burning of a disrupted, lower-density secondary WD.

5. Our spectrum of SN 2022pul is quite well matched by the MERGER model nebular spectrum computed by Blondin et al. (2023) from the violent WD–WD merger model of Pakmor et al. (2012). The agreement between the observed and model spectra is further improved by the addition of clumping and 0.1 $M_\odot$ to the central mass.

6. It is still somewhat unclear how the violent merger model can produce both the C/O-rich CSM described by Paper I (Siebert et al. 2024) and Paper III (J. Johansson et al. 2024, in preparation), and the central O and Ne seen in the spectra.

7. Further work and more detailed models are needed to constrain the masses of the WDs involved in the merger.

Our observations of SN 2022pul are a prime example of the importance of gathering spectra of WD SNe across the optical, NIR, and MIR wavelengths. The MIR observation of [Ne II] is complementary to the observation of [O I] in the optical; the optical [Ca II], NIR [Ca IV], and MIR [Ar II], [Ar III], and [S IV] mutually help interpret the IME distribution and ionization stratification; and the NIR [Fe II] and MIR [Co III] lines establish the distribution of the IGEs. Furthermore, the higher-resolution ground-based optical and NIR observations were essential to interpret the lower-resolution JWST observations, and isolated MIR spectral lines were key to unraveling the complex line blending in the optical and NIR.

Future observations of 03fg-like SNe Ia would benefit from JWST spectroscopy, especially in the higher-resolution instrument modes which reach to even longer wavelengths and reveal additional lines. Complementary spectropolarimetry would give insight into line-profile asymmetries and constrain aspect angles (DerKacy et al. 2023). If this class of objects indeed arises from WD mergers, the observations should show a large degree of diversity in their asymmetric line profiles, and JWST observations could additionally establish a firmer connection to the dust surrounding or formed in these objects.

Facilities: AAVSO, ATT (WiFeS), ASAS-SN, ATLAS, GTC (OSIRIS), JWST (NIRSpec/MIRI), Keck:I (LRIS), Keck:II (NIRES), Keck:II (DEIMOS), LCO/GSP, Magellan: Baade (IMACS), MMT (Binospec), SALT (RSS), Shane (Kast), SOAR (Goodman), Subaru (FOCAS), UH:2.2m (SNIFS), and PO:1.2m (ZTF).

Software: Astropy (Astropy Collaboration et al. 2013, 2018, 2022), Matplotlib (Hunter 2007), NumPy (Oliphant 2006), PyRAF (Science Software Branch at STScI 2012), PySALT (Crawford et al. 2010), dust extinction (Gordon et al. 2022), jdaviz (JDADF Developers et al. 2022), jwst (Bushouse et al. 2022), UltraNest (Buchner 2021; Buchner et al. 2022), YSE-PZ (Coulter et al. 2022, 2023), and CMFGEN (Hillier & Dessart 2012).

ORCID iDs

Lindsey A. Kwok ⓘ https://orcid.org/0000-0003-3108-1328
Matthew R. Siebert ⓘ https://orcid.org/0000-0003-2445-3891
Joel Johansson ⓘ https://orcid.org/0000-0001-5975-290X
Saurabh W. Jha ⓘ https://orcid.org/0000-0001-8738-6011
Stéphane Blondin ⓘ https://orcid.org/0000-0002-9388-2932
Luc Dessart ⓘ https://orcid.org/0000-0003-0599-8407
Ryan J. Foley ⓘ https://orcid.org/0000-0002-2445-5275
D. John Hillier ⓘ https://orcid.org/0000-0001-5094-8017
Conor Larison ⓘ https://orcid.org/0000-0003-2037-4619
Rüdiger Pakmor ⓘ https://orcid.org/0000-0003-3308-2420
Tea Temim ⓘ https://orcid.org/0000-0001-7380-3144
Jennifer E. Andrews ⓘ https://orcid.org/0000-0003-0123-0062
Katie Auchettl ⓘ https://orcid.org/0000-0002-4449-9152
Carles Badenes ⓘ https://orcid.org/0000-0003-3494-343X
Barna Barnabas ⓘ https://orcid.org/0000-0003-4769-4794
K. Azalee Bostroem ⓘ https://orcid.org/0000-0002-4924-444X
Max J. Brenner Newman ⓘ https://orcid.org/0000-0002-8092-2077

Thomas G. Brink ⓘ https://orcid.org/0000-0001-5955-2502
María José Bustamante-Rosell ⓘ https://orcid.org/0000-0003-0416-9818
Yssavo Camacho-Neves ⓘ https://orcid.org/0000-0002-9830-3880
Alejandro Clocchiatti ⓘ https://orcid.org/0000-0003-3068-4258
David A. Coulter ⓘ https://orcid.org/0000-0003-4263-2228
Kyle W. Davis ⓘ https://orcid.org/0000-0002-5680-4660
Maxime Deckers ⓘ https://orcid.org/0000-0001-8857-9843
Georgios Dimitriadis ⓘ https://orcid.org/0000-0001-9494-179X
Yize Dong ⓘ https://orcid.org/0000-0002-7937-6371
Joseph Farah ⓘ https://orcid.org/0000-0003-4914-5625
Alexei V. Filippenko ⓘ https://orcid.org/0000-0003-3460-0103
Andreas Flörs ⓘ https://orcid.org/0000-0003-2024-2819
Ori D. Fox ⓘ https://orcid.org/0000-0003-2238-1572
Peter Garnavich ⓘ https://orcid.org/0000-0003-4069-2817
Estefania Padilla Gonzalez ⓘ https://orcid.org/0000-0003-0209-9246
Or Graur ⓘ https://orcid.org/0000-0002-4391-6137
Franz-Josef Hambsch ⓘ https://orcid.org/0000-0003-0125-8700
Griffin Hosseinzadeh ⓘ https://orcid.org/0000-0002-0832-2974
D. Andrew Howell ⓘ https://orcid.org/0000-0003-4253-656X
John P. Hughes ⓘ https://orcid.org/0000-0002-8816-6800
Wolfgang E. Kerzendorf ⓘ https://orcid.org/0000-0002-0479-7235
Xavier K. Saux ⓘ https://orcid.org/0009-0004-3242-282X
Keiichi Maeda ⓘ https://orcid.org/0000-0003-2611-7269
Kate Maguire ⓘ https://orcid.org/0000-0002-9770-3508
Curtis McCully ⓘ https://orcid.org/0000-0001-5807-7893
Cassidy Mihalenko ⓘ https://orcid.org/0009-0004-0322-6299
Megan Newsome ⓘ https://orcid.org/0000-0001-9570-0584
John T. O'Brien ⓘ https://orcid.org/0000-0003-3615-9593
Jeniveve Pearson ⓘ https://orcid.org/0000-0002-0744-0047
Craig Pellegrino ⓘ https://orcid.org/0000-0002-7472-1279
Justin D. R. Pierel ⓘ https://orcid.org/0000-0002-2361-7201
Abigail Polin ⓘ https://orcid.org/0000-0002-1633-6495
Armin Rest ⓘ https://orcid.org/0000-0002-4410-5387
César Rojas-Bravo ⓘ https://orcid.org/0000-0002-7559-315X
David J. Sand ⓘ https://orcid.org/0000-0003-4102-380X
Michaela Schwab ⓘ https://orcid.org/0009-0002-5096-1689
Melissa Shahbandeh ⓘ https://orcid.org/0000-0002-9301-5302
Manisha Shrestha ⓘ https://orcid.org/0000-0002-4022-1874
Nathan Smith ⓘ https://orcid.org/0000-0001-5510-2424
Louis-Gregory Strolger ⓘ https://orcid.org/0000-0002-7756-4440
Tamás Szalai ⓘ https://orcid.org/0000-0003-4610-1117
Kirsty Taggart ⓘ https://orcid.org/0000-0002-5748-4558
Giacomo Terreran ⓘ https://orcid.org/0000-0003-0794-5982
Jacco H. Terwel ⓘ https://orcid.org/0000-0001-9834-3439
Samaporn Tinyanont ⓘ https://orcid.org/0000-0002-1481-4676
Stefano Valenti ⓘ https://orcid.org/0000-0001-8818-0795
József Vinkó ⓘ https://orcid.org/0000-0001-8764-7832
J. Craig Wheeler ⓘ https://orcid.org/0000-0003-1349-6538
Yi Yang ⓘ https://orcid.org/0000-0002-6535-8500
WeiKang Zheng ⓘ https://orcid.org/0000-0002-2636-6508
Chris Ashall ⓘ https://orcid.org/0000-0002-5221-7557

James M. DerKacy ⬤ https://orcid.org/0000-0002-7566-6080
Lluís Galbany ⬤ https://orcid.org/0000-0002-1296-6887
Peter Hoeflich ⬤ https://orcid.org/0000-0002-4338-6586
Thomas de Jaeger ⬤ https://orcid.org/0000-0001-6069-1139
Jing Lu ⬤ https://orcid.org/0000-0002-3900-1452
Justyn Maund ⬤ https://orcid.org/0000-0003-0733-7215
Kyle Medler ⬤ https://orcid.org/0000-0001-7186-105X
Nidia Morell ⬤ https://orcid.org/0000-0003-2535-3091
Benjamin J. Shappee ⬤ https://orcid.org/0000-0003-4631-1149
Maximilian Stritzinger ⬤ https://orcid.org/0000-0002-5571-1833
Nicholas Suntzeff ⬤ https://orcid.org/0000-0002-8102-181X
Michael Tucker ⬤ https://orcid.org/0000-0002-2471-8442
Lifan Wang ⬤ https://orcid.org/0000-0001-7092-9374

References

Ashall, C., Lu, J., Hsiao, E. Y., et al. 2021, ApJ, 922, 205
Astropy Collaboration, Price-Whelan, A. M., Lim, P. L., et al. 2022, ApJ, 935, 167
Astropy Collaboration, Price-Whelan, A. M., Sipőcz, B. M., et al. 2018, AJ, 156, 123
Astropy Collaboration, Robitaille, T. P., Tollerud, E. J., et al. 2013, A&A, 558, A33
Axelrod, T. S. 1980, PhD thesis, Univ. of California, Santa Cruz
Benetti, S., Cappellaro, E., Mazzali, P. A., et al. 2005, ApJ, 623, 1011
Black, C. S., Fesen, R. A., & Parrent, J. T. 2016, MNRAS, 462, 649
Blondin, S., Dessart, L., Hillier, D. J., Ramsbottom, C. A., & Storey, P. J. 2023, A&A, 678, 30
Bora, Z., Vinkó, J., & Könyves-Tóth, R. 2022, PASP, 134, 054201
Botyánszki, J., Kasen, D., & Plewa, T. 2018, ApJL, 852, L6
Bowers, E. J. C., Meikle, W. P. S., Geballe, T. R., et al. 1997, MNRAS, 290, 663
Branch, D., Jeffery, D. J., Parrent, J., et al. 2008, PASP, 120, 135
Branch, D., & Wheeler, J. C. 2017, Supernova Explosions (Berlin: Springer), 82
Buchner, J. 2021, JOSS, 6, 3001
Buchner, J., Ball, W., Smirnov-Pinchukov, G., Nitz, A., & Susemiehl, N. 2022, JohannesBuchner/UltraNest: v3.5.0, Zenodo, doi:10.5281/zenodo.7053560
Bulla, M., Sim, S. A., Pakmor, R., et al. 2016, MNRAS, 455, 1060
Bushouse, H., Eisenhamer, J., Dencheva, N., et al. 2022, JWST Calibration Pipeline v1.11.1, Zenodo, doi:10.5281/zenodo.7038885
Cikota, A., Patat, F., Wang, L., et al. 2019, MNRAS, 490, 578
Coulter, D. A., Jones, D. O., McGill, P., et al. 2022, YSE-PZ: An Open-source Target and Observation Management System, v0.3.0, Zenodo, doi:10.5281/zenodo.7278430
Coulter, D. A., Jones, D. O., McGill, P., et al. 2023, PASP, 135, 064501
Crawford, S. M., Still, M., Schellart, P., et al. 2010, Proc. SPIE, 7737, 25
DerKacy, J. M., Ashall, C., Hoeflich, P., et al. 2023, ApJL, 945, L2
Dessart, L., Hillier, D. J., Sukhbold, T., Woosley, S. E., & Janka, H. T. 2021, A&A, 652, A64
Dessart, L., Leonard, D. C., & Prieto, J. L. 2020, A&A, 638, A80
Dimitriadis, G., Foley, R. J., Arendse, N., et al. 2022, ApJ, 927, 78
Dimitriadis, G., Maguire, K., Karambelkar, V. R., et al. 2023, MNRAS, 521, 1162
Filippenko, A. V., Matheson, T., & Barth, A. J. 1994, AJ, 108, 2220
Filippenko, A. V., & Sargent, W. L. W. 1989, ApJL, 345, L43
Fink, M., Kromer, M., Seitenzahl, I. R., et al. 2014, MNRAS, 438, 1762
Flörs, A., Spyromilio, J., Maguire, K., et al. 2018, A&A, 620, A200
Flörs, A., Spyromilio, J., Taubenberger, S., et al. 2020, MNRAS, 491, 2902
Foley, R. J., Challis, P. J., Chornock, R., et al. 2013, ApJ, 767, 57
Friesen, B., Baron, E., Wisniewski, J. P., et al. 2014, ApJ, 792, 120
Gordon, K., Larson, K., McBride, A., et al. 2022, karllark/dust_extinction: NIRSpectralExtinctionAdded, v1.1, Zenodo, doi:10.5281/zenodo.6397654
Grishin, E., & Perets, H. B. 2022, MNRAS, 512, 4993
Gronow, S., Collins, C. E., Sim, S. A., & Röpke, F. K. 2021, A&A, 649, A155
Guillochon, J., Dan, M., Ramirez-Ruiz, E., & Rosswog, S. 2010, ApJL, 709, L64
Hicken, M., Garnavich, P. M., Prieto, J. L., et al. 2007, ApJL, 669, L17
Hillier, D. J., & Dessart, L. 2012, MNRAS, 424, 252
Hoeflich, P., Khokhlov, A., Wheeler, J. C., et al. 1996, ApJL, 472, L81
Houck, J. C., & Fransson, C. 1996, ApJ, 456, 811
Howell, D. A., Sullivan, M., Nugent, P. E., et al. 2006, Natur, 443, 308
Hsiao, E. Y., Hoeflich, P., Ashall, C., et al. 2020, ApJ, 900, 140
Hunter, J. D. 2007, CSE, 9, 90
JDADF Developers, Averbukh, J., Bradley, L., et al. 2022, Jdaviz, v3.1.0, Zenodo, doi:10.5281/zenodo.7255461
Jerkstrand, A. 2017, in Handbook of Supernovae, ed. A. W. Alsabti & P. Murdin (Berlin: Springer), 795
Jha, S. W., Maguire, K., & Sullivan, M. 2019, NatAs, 3, 706
Kashi, A., & Soker, N. 2011, MNRAS, 417, 1466
Khokhlov, A., Mueller, E., & Hoeflich, P. 1993, A&A, 270, 223
Kozma, C., Fransson, C., Hillebrandt, W., et al. 2005, A&A, 437, 983
Kromer, M., Pakmor, R., Taubenberger, S., et al. 2013, ApJL, 778, L18
Kushnir, D., Katz, B., Dong, S., Livne, E., & Fernández, R. 2013, ApJL, 778, L37
Kwok, L. A., Jha, S. W., Temim, T., et al. 2023, ApJL, 944, L3
Lach, F., Callan, F. P., Sim, S. A., & Röpke, F. K. 2022, A&A, 659, A27
Liu, Z.-W., Röpke, F. K., & Han, Z. 2023, RAA, 23, 082001
Livio, M., & Riess, A. G. 2003, ApJL, 594, L93
Lu, J., Ashall, C., Hsiao, E. Y., et al. 2021, ApJ, 920, 107
Maeda, K., Jiang, J.-a., Doi, M., Kawabata, M., & Shigeyama, T. 2023, MNRAS, 521, 1897
Maguire, K., Sim, S. A., Shingles, L., et al. 2018, MNRAS, 477, 3567
Marietta, E., Burrows, A., & Fryxell, B. 2000, ApJS, 128, 615
Moll, R., & Woosley, S. E. 2013, ApJ, 774, 137
Nadyozhin, D. K. 1994, ApJS, 92, 527
Noebauer, U. M., Taubenberger, S., Blinnikov, S., Sorokina, E., & Hillebrandt, W. 2016, MNRAS, 463, 2972
Oliphant, T. E. 2006, A Guide to NumPy (Trelgol Publishing: USA)
Pakmor, R. 2017, in Handbook of Supernovae, ed. A. W. Alsabti & P. Murdin (Berlin: Springer), 1257
Pakmor, R., Hachinger, S., Röpke, F. K., & Hillebrandt, W. 2011, A&A, 528, A117
Pakmor, R., Kromer, M., Röpke, F. K., et al. 2010, Natur, 463, 61
Pakmor, R., Kromer, M., Taubenberger, S., & Springel, V. 2013, ApJL, 770, L8
Pakmor, R., Kromer, M., Taubenberger, S., et al. 2012, ApJL, 747, L10
Phillips, M. M. 1993, ApJL, 413, L105
Quimby, R., Höflich, P., & Wheeler, J. C. 2007, ApJ, 666, 1083
Rajamuthukumar, A. S., Hamers, A. S., Neunteufel, P., Pakmor, R., & de Mink, S. E. 2023, ApJ, 950, 9
Raskin, C., & Kasen, D. 2013, ApJ, 772, 1
Scalzo, R. A., Aldering, G., Antilogus, P., et al. 2010, ApJ, 713, 1073
Science Software Branch at STScI, 2012 PyRAF: Python alternative for IRAF, Astrophysics Source Code Library, ascl:1207.011
Seitenzahl, I. R., Ciaraldi-Schoolmann, F., Röpke, F. K., et al. 2013, MNRAS, 429, 1156
Siebert, M. R., Foley, R. J., Zenati, Y., et al. 2023, ApJ, 960, 19
Siebert, M. R., Kwok, L. A., Johansson, J., et al. 2024, ApJ, 960, 88
Silverman, J. M., Ganeshalingam, M., Li, W., et al. 2011, MNRAS, 410, 585
Silverman, J. M., Nugent, P. E., Gal-Yam, A., et al. 2013, ApJS, 207, 3
Srivastav, S., Smartt, S. J., Huber, M. E., et al. 2023, ApJL, 943, L20
Tanaka, M., Kawabata, K. S., Yamanaka, M., et al. 2010, ApJ, 714, 1209
Taubenberger, S. 2017, in Handbook of Supernovae, ed. A. W. Alsabti & P. Murdin (Berlin: Springer), 317
Taubenberger, S., Floers, A., Vogl, C., et al. 2019, MNRAS, 488, 5473
Taubenberger, S., Kromer, M., Hachinger, S., et al. 2013, MNRAS, 432, 3117
van Kerkwijk, M. H., Chang, P., & Justham, S. 2010, ApJL, 722, L157
Wang, L. 2005, ApJL, 635, L33
Yoon, S. C., & Langer, N. 2005, A&A, 435, 967